Draft version May 16, 2024
Typeset using LaTeX default style in AASTeX62

PUSHING THE LIMITS OF THE COSMIC ORIGIN SPECTROGRAPH (COS) WITH AN OPTIMIZED BACKGROUND CORRECTION: A DETAILED CHARACTERIZATION

Svea Hernandez,[1] Andrei Igoshev,[2] Jo Taylor,[3] David Sahnow,[3] and Logan Jones[3]

[1] *AURA for ESA, Space Telescope Science Institute, 3700 San Martin Drive, Baltimore, MD 21218, USA*
[2] *Department of Applied Mathematics, University of Leeds, Leeds LS2 9JT, UK*
[3] *Space Telescope Science Institute, 3700 San Martin Drive, Baltimore, MD 21218, USA*

1. FULL CHARACTERIZATION OF THE COS BACKGROUND

Studies have observed strong correlations between the COS FUV dark rates and solar activity. Other possible correlations with the detector background include detector gain and HV (e.g., Johnson 2023).

1.1. *Solar Flux*

Given that the dark rate of the COS FUV segments is known to vary spatially and with time, we investigated the variations in the dark counts registered in the inner region as a function of solar activity. We note that for this work we use the 10.7 cm solar flux tracked by the National Oceanic and Atmospheric Administration (NOAA[1]) as a proxy for solar activity.

We estimated the Pearson product-moment correlation coefficient (Pearson 1948) for both COS segments to assess if there is a statistical correlation between solar flux and dark counts. These correlation coefficients describe the degree at which a given variable changes in relation to another one. In Figure 1 we show the total dark counts registered in the COS inner region (stored in the `SQLite` database) for segment A and B with HVs of 167 and 175, respectively, as a function of solar flux. Each individual event registered by the COS detector is recorded to have a specific PHA, with values ranging between 0 and 31 (inclusive). Figure 1 includes all registered counts, without filtering on PHA values (see Section 1.2). We calculate a correlation coefficient of 0.40 for segment A, and 0.20 for segment B. These values indicate that there is an apparent correlation in segment A, however, such a trend is much more uncertain in segment B across all HVs.

1.2. *Pulse Height Amplitude (PHA)*

For each photon that lands on the COS FUV detectors, a cascade of electrons is created which is characterized by a PHA that is then registered by the electronics (see Section 4.1.7 in Hirschauer 2023). It has been generally understood that external events are distinguished from background noise events by their PHA values, where dark events typically have low PHAs (PHA = 0 - 2) and real/external events register higher PHA values (PHA $\geq$ 3). As noted in Sahnow et al. (2011), background counts are expected to display a negative exponential pulse height distribution (PHD). In contrast, the PHD observed for photon events is more commonly quasi-gaussian.

We inspected the PHD of the dark counts stored in the `SQLite` database for different periods of time, observed while solar fluxes varied from low to high values. Our analysis showed slightly different trends than those detailed by Sahnow et al. (2011). In Figure 3 we show the PHDs of a dark exposure taken while solar activity appeared to be low (or quiescent, with fluxes of the order of $\sim 77 \times 10^{-22}$ W m^{-2} Hz^{-1}) as tracked by solar radio fluxes (top panels). These trends are to be contrasted with the PHDs observed while solar activity was recorded to be high (solar fluxes of the order of $\sim 130 \times 10^{-22}$ W m^{-2} Hz^{-1} ; bottom panels). The top panels in Figure 3 clearly highlight the different trends observed in the two segments. While the PHDs in segment A follow negative exponential trends as expected, segment B appears to have a much flatter (or even positive exponential) trend. This overall trend remains consistent for segment B even during those periods of time where solar activity appears to be higher than nominal (lower left panel in Figure 3). The PHD in segment A observed during high solar fluxes appears to display a much more complex pattern, one that is better reproduced by a combination of an exponential and normal distribution.

Corresponding author: Svea Hernandez
sveash@stsci.edu

[1] https://www.swpc.noaa.gov/products/solar-cycle-progression

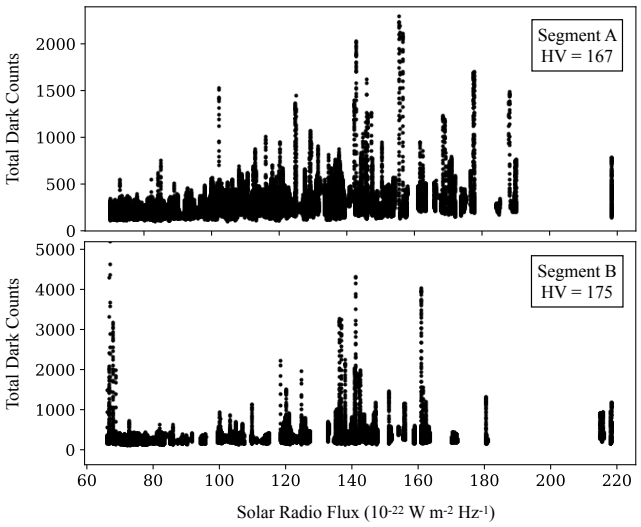

Figure 1. COS dark counts as a function of solar radio flux. We use the 10.7 cm solar flux tracked by NOAA as a proxy for solar activity. Top: dark counts registered in segment A using a HV of 167. Bottom: dark counts registered in segment B using a HV of 175.

To characterize the PHDs, we fit two different trends: (1) exponential distribution and (2) exponential and normal distributions combined. The exponential distribution model is defined as

$$f(i) = A \exp\left(-\frac{i}{E_t}\right), \tag{1}$$

where A is the normalization factor and E_t is the rate at which the number of events changes with respect to PHA (i.e., describes how fast the number of dark photons decreases with PHA).

The second model, combined exponential and normal distributions, is described as follows

$$f(i) = A \exp\left(-\frac{i}{E_t}\right) + B \exp\left(-\frac{(i-\mu)^2}{2\sigma^2}\right) \tag{2}$$

where μ is the mean value (peak of the normal component) and σ is the width of the normal component. B is the contribution of the normal distribution, which should be compared to A. To infer the different values and characterize the PHDs we minimize the likelihood function, and use C-statistics (Cash 1979) to assess how accurate the different models are at correctly classifying the PHDs, and to select the best model. In Figure 3 we show in blue their best fits. We note that we excluded PHA values of 0 and 31 when fitting the model, as these PHA values have been historically excluded by the standard pipeline (Syphers & Shull 2013). Given the much stronger correlation between dark counts and solar flux observed in segment A, compared to the trend in segment B, we investigated a possible correlation between coefficients A and B in equation 2 using a suite of dark exposures. A comparison of these two coefficients provides information on which of the two components is dominating the dark counts at a given point in time, the exponential component (tracked by the A coefficient), or the normal distribution component (tracked by the B coefficient).

In the top panel of Figure 4 we show the ratio of B/A coefficients, as a function of time (in Modified Julian Day, MJD) for segment A and HV = 167. The shaded regions highlight the periods of time where the PHD is dominated by the normal distribution, as opposed to the exponential component. The apparent peaks observed in the B/A values, are much higher than the observed dispersion in the rest of the points. The peaks in the B/A values typically occur throughout an extensive period of time when solar activity was recorded to be higher than nominal (bottom panel in Figure 4). We note that such a trend is absent in the B/A values for segment B. Instead, a similar plot as Figure 4 including the information for segment B only shows large scatter with values ranging between $B/A \sim 0$ - 2.

In summary, our analysis indicated drastically different behavior in the PHDs of the two COS segments, where the PHD for segment B exhibited a similar trend (that of an exponential distribution) irrespective of time and/or solar activity. The PHD for segment A is slightly more complicated where at different epochs the PHDs showed

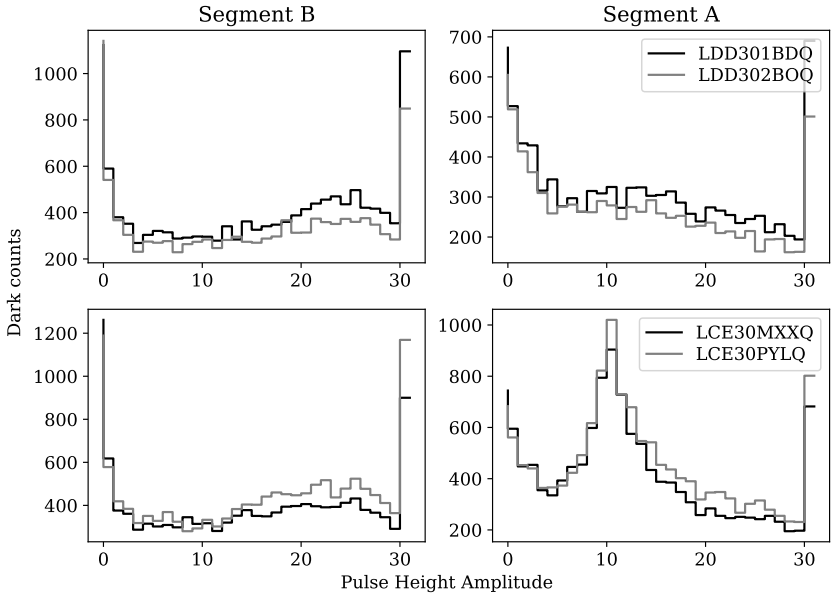

Figure 2. Dark counts as a function of pulse height amplitude (PHA) as observed in several different dark exposures. We show on the left panels the dark counts registered on segment B, and on the right panels the dark counts recorded on segment A. Top panels: Dark exposures taken on October 2016, with radio solar fluxes of the order of $\sim 77 \times 10^{-22}$ W m^{-2} Hz^{-1}. Bottom panels: Dark exposures taken on November 2013, with radio solar fluxes of the order of $\sim 130 \times 10^{-22}$ W m^{-2} Hz^{-1}.

a combination of exponential and normal distributions together, with the normal distributions dominating over the exponential function.

1.3. *Spatial variations*

As detailed in the previous section, our PHA analysis showed that generally when solar activity registered high radio fluxes, the PHDs of the dark counts were typically dominated by a normal distribution, specifically for segment A. Furthermore, for those exposures where the normal distribution dominated over the exponential function, the PHDs appear to peak around PHA values $\sim$11 (see lower right panel in Figures 2 and 3; the peak value varied slightly depending on HV). Note that the PHA peak of the normal distribution of dark counts differed from the normal distribution from photon events (i.e. astronomical objects). To investigate if there were any spatial-variation trends in the 2D dark exposures, we created 2D images where we highlight the dark counts for a given PHA value.

We show the 2D images of segments A and B for exposures LDD301BDQ (low solar activity) and LCE30MXXQ (high solar activity) in Figures 5-8. The HV values used are 167 and 169 for segment A and B, respectively. These figures show the spatial differences in the recorded dark counts for a given PHA value (pink points), and for a combination of PHAs (black points), including all PHAs (0-31) as well as PHAs used by `CalCOS` (PHAs 2-23). The contrast between low and high background activity is particularly dramatic for segment A. Overall, with the exception of PHA=31 in segment B, the spatial distribution of the dark counts in both segments at each PHA value lacks any "bright" structure in the exposures taken while solar activity was low (Figures 5 and 6). On the other hand, the dark counts for segment A with PHA = 10 - 12 appear to be more localized in the middle of the detector exhibiting a sort of "glow" structure running from the upper to lower regions. It is clear that a large fraction of the counts from the normal distribution in Figures 2 and 3 exhibit a peculiar and localized spatial trend.

Lastly, although we note that there is very little difference in structure in the images for segment B between low and high solar activity periods, we identified a sort of "banding/striping", in both segment B frames. While faint, this effect begins appearing at PHA$\sim$27 and is suspected to be caused by inaccurate corrections to geometric distortion and walk (Sahnow et al. 2016). This "banding/striping" effect is more evident when coadding individual darks, see Figures 11 and 12.

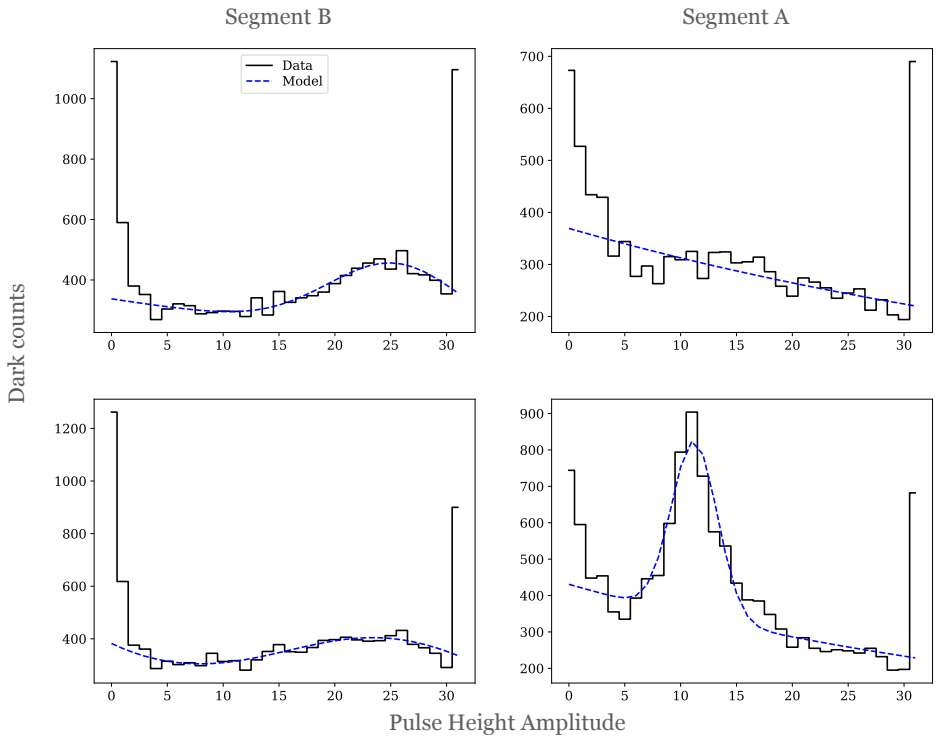

Figure 3. Dark counts as a function of pulse height amplitude (PHA). The two left panels display the PHA values in segment B. The two right panels display the PHA values registered in segment A. We show with a blue dashed line the inferred best model according to c-statistics, following either equation 1 (e.g., top right panel) or 2 (e.g., bottom right panel). Top panels: Dark counts recorded during low solar activity as part of COS dark exposure LDD301BDQ. Bottom panels: Dark counts recorded during high solar activity as part of COS dark exposure LCE30MXXQ.

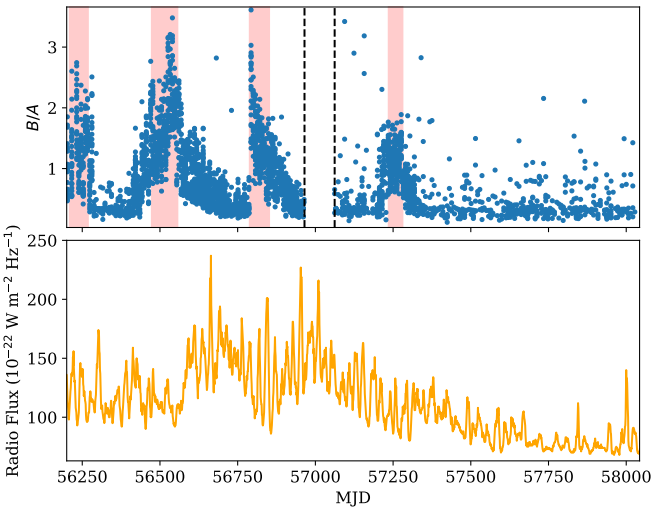

Figure 4. *Top:* Ratio of B/A coefficients as a function of time (in MJD) for segment A and HV = 167. The dashed vertical lines mark the period in time where the HV was temporarily changed from HV = 167 to HV =175. The shaded regions indicate the epochs where the PHDs of the dark exposures are dominated by the B component (e.g., normal distribution), instead of the exponential trend. *Bottom:* Solar Flux as a function of time (MJD).

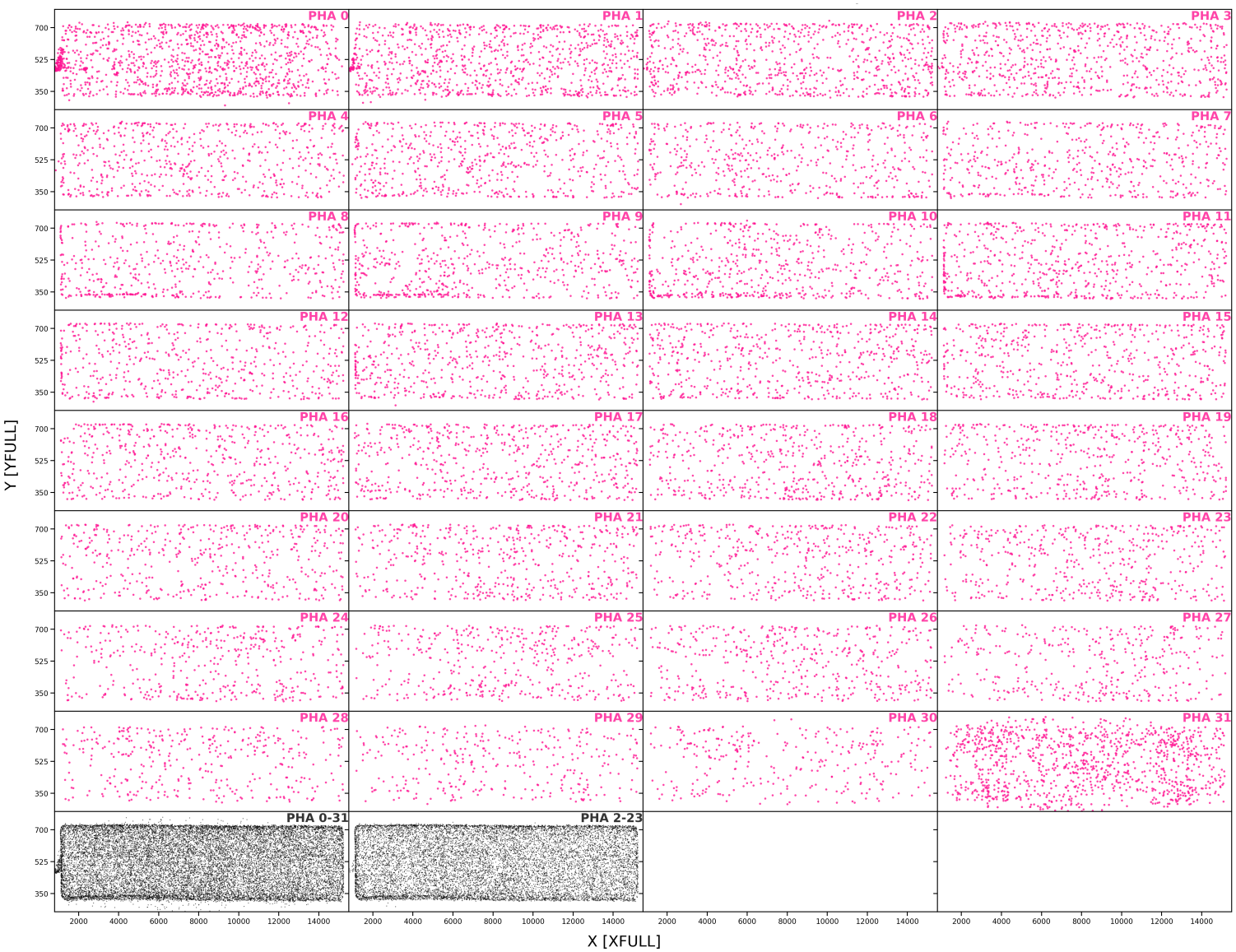

Figure 5. Dark exposure LDD301BDQ for segment A taken during a low solar activity period (Oct 31, 2016; HV=167). The counts for the different PHA values are shown in magenta in each panel. The lower panels show the combined counts with PHA ranges indicated in the legend.

REFERENCES

Cash, W. 1979, ApJ, 228, 939, doi: 10.1086/156922

Hirschauer, A. S. 2023, in COS Instrument Handbook v. 16.0, Vol. 16, 16

Johnson, C. I. 2023, Cycle 29 COS FUV Dark Monitor Summary, Instrument Science Report COS 2023-22, 9 pages

Pearson, K. 1948, Karl Pearson's Early Statistical Papers (Cambridge University Press). https://books.google.com/books?id=GHlhtAEACAAJ

Sahnow, D. J., Oliveira, C., Aloisi, A., et al. 2011, in Society of Photo-Optical Instrumentation Engineers (SPIE) Conference Series, Vol. 8145, Society of Photo-Optical Instrumentation Engineers (SPIE) Conference Series, 81450Q

Sahnow, D. J., Penton, S., Ake, T., et al. 2016, in Society of Photo-Optical Instrumentation Engineers (SPIE) Conference Series, Vol. 9905, Space Telescopes and Instrumentation 2016: Ultraviolet to Gamma Ray, ed. J.-W. A. den Herder, T. Takahashi, & M. Bautz, 99052T

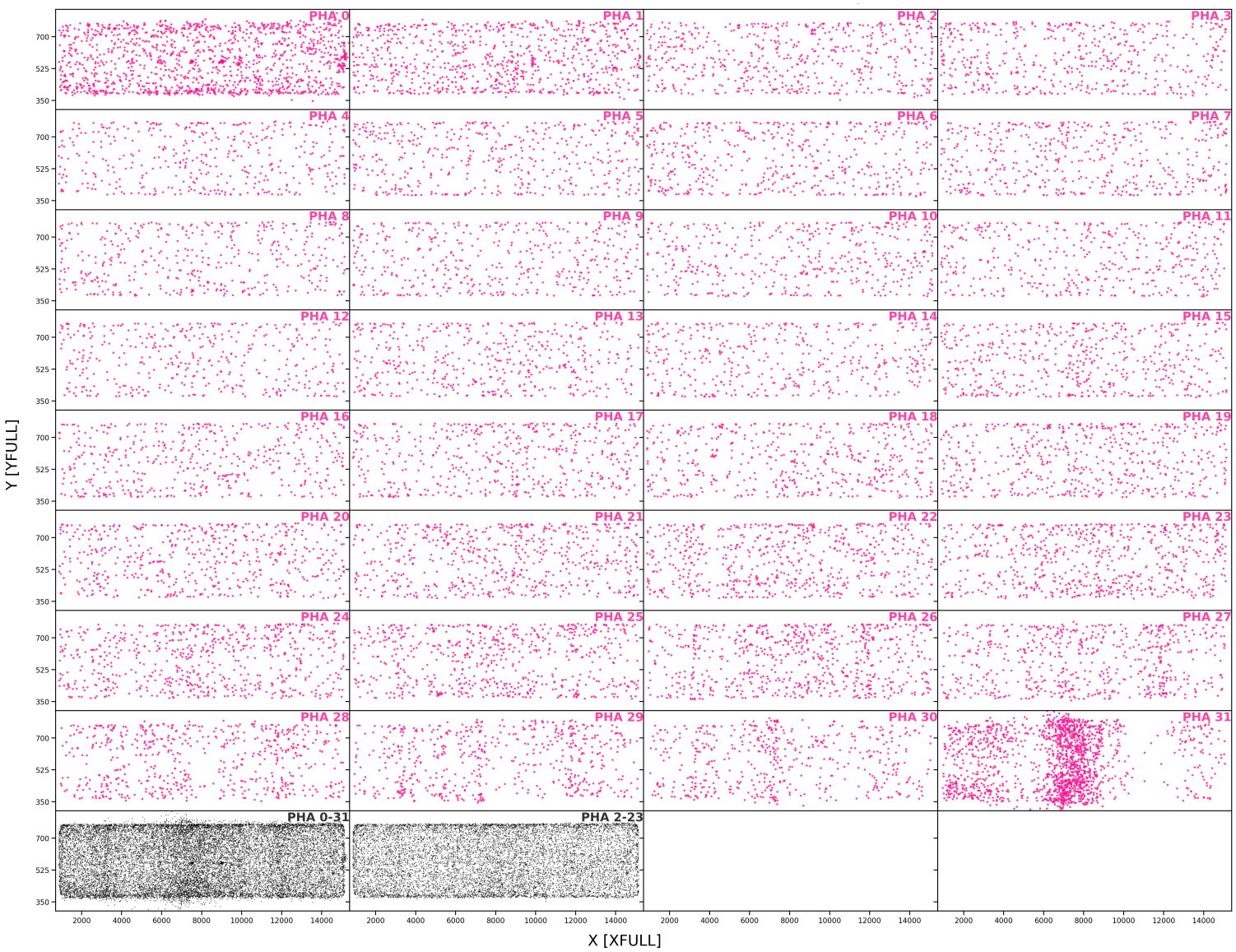

Figure 6. Dark exposure LDD301BDQ for segment B taken during a low solar activity period (Oct 31, 2016; HV=175). The counts for the different PHA values are shown in magenta in each panel. The lower panels show the combined counts with PHA ranges indicated in the legend.

Syphers, D., & Shull, J. M. 2013, ApJ, 765, 119,
doi: 10.1088/0004-637X/765/2/119

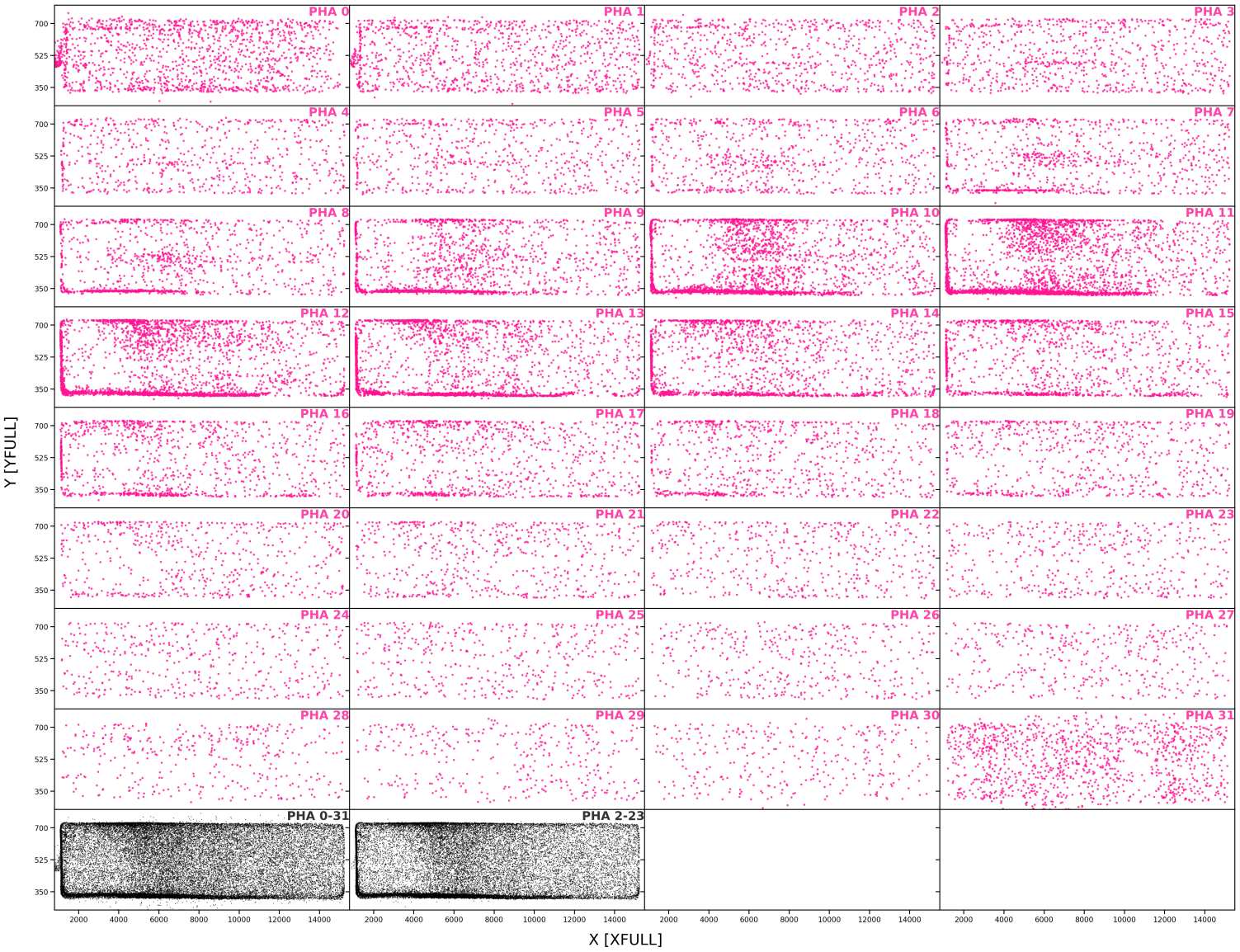

Figure 7. Dark exposure LCE30MXXQ for segment A taken during a high solar activity period (Nov 29, 2013; HV=167). The counts for the different PHA values are shown in magenta in each panel. The lower panels show the combined counts with PHA ranges indicated in the legend.

APPENDIX

A. PHA-DEPENDENT SUPERDARK FEATURES

We show in this document the 2D images of different superdarks as a function of PHA (Figures 13-36). These figures highlight how some particular dark structures originate and evolve at specific PHA values. The origin of most of these features is still unknown.

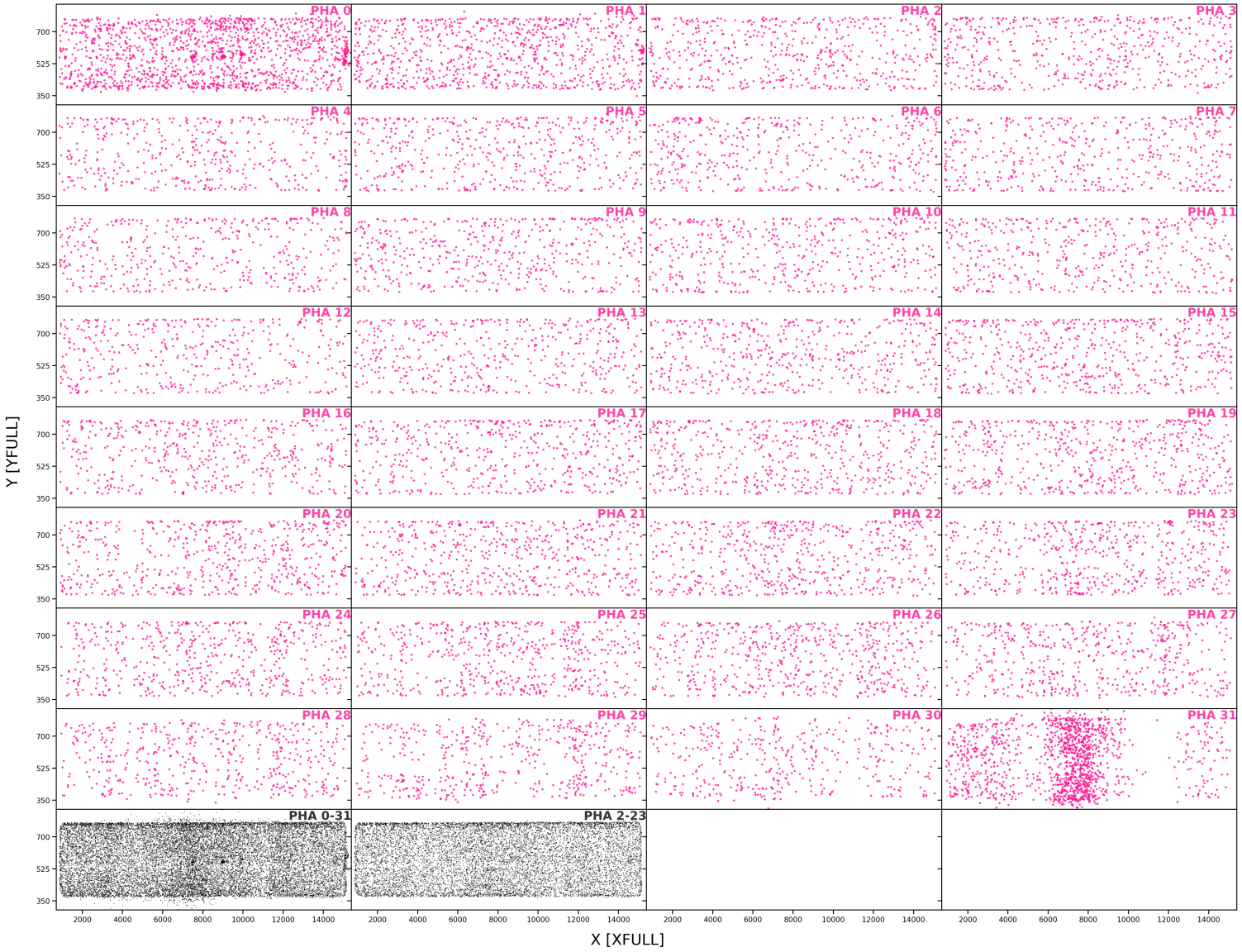

Figure 8. Dark exposure LCE30MXXQ for segment A taken during a high solar activity period (Nov 29, 2013; HV=167). The counts for the different PHA values are shown in magenta in each panel. The lower panels show the combined counts with PHA ranges indicated in the legend.

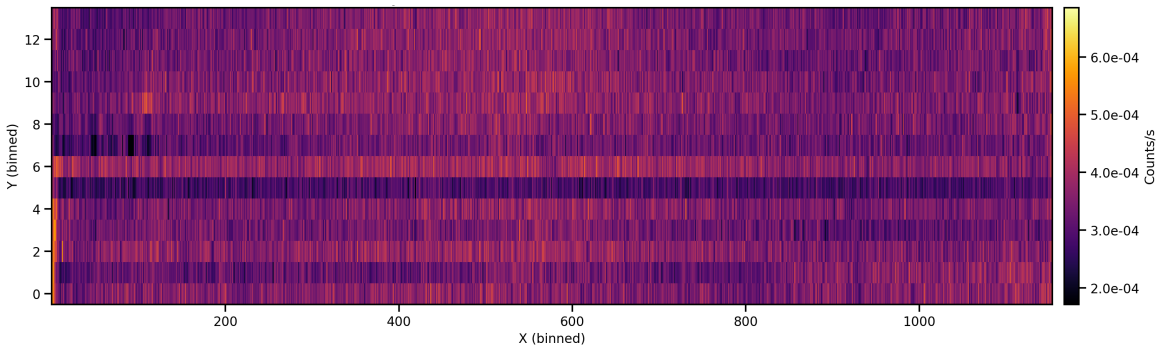

Figure 9. Superdark for segment A taken with HV=167. The image was created through a compilation of individual dark exposures taken during periods of time where solar activity was relatively low. The superdark was heavily smoothed and binned from the original 16,384 × 1,024 pixels to 1,154 × 14 superpixels. Note the heavily sagged region at row 5.

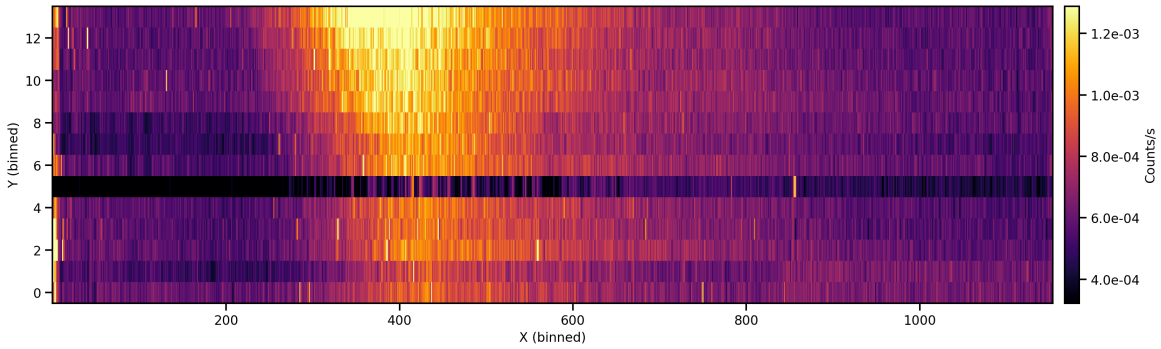

Figure 10. Similar to Figure 9 but using dark exposures taken during high background activity. Note the bright yellow structure appearing on the top of the detector with an over density of counts, decreasing towards the bottom of the detector. This pattern is absent in the segment B superdark for the high activity state. We highlight the heavily sagged region at row 5, as well as the difference in color scale compared to Figure 9.

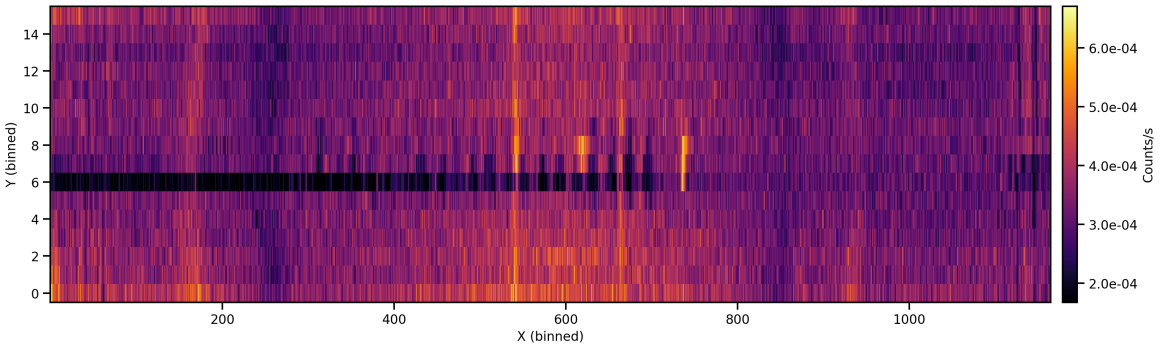

Figure 11. Superdark for segment B taken with HV=169. The image was created through a compilation of individual dark exposures taken during periods of time where solar activity was relatively low. The superdark was heavily smoothed and binned from the original 16,384 × 1,024 pixels to 1,165 × 16 superpixels.

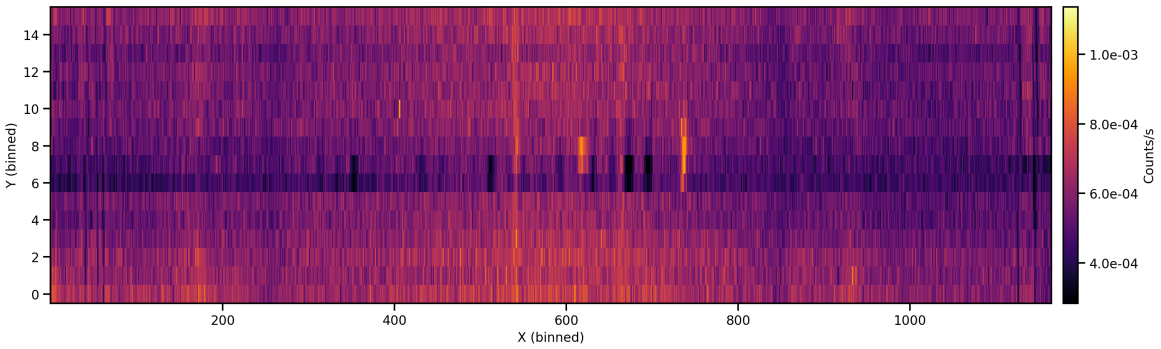

Figure 12. Similar to Figure 11 but using dark exposures taken during high background activity. We highlight the sagged region at row 6, as well as the difference in color scale compared to Figure 11.

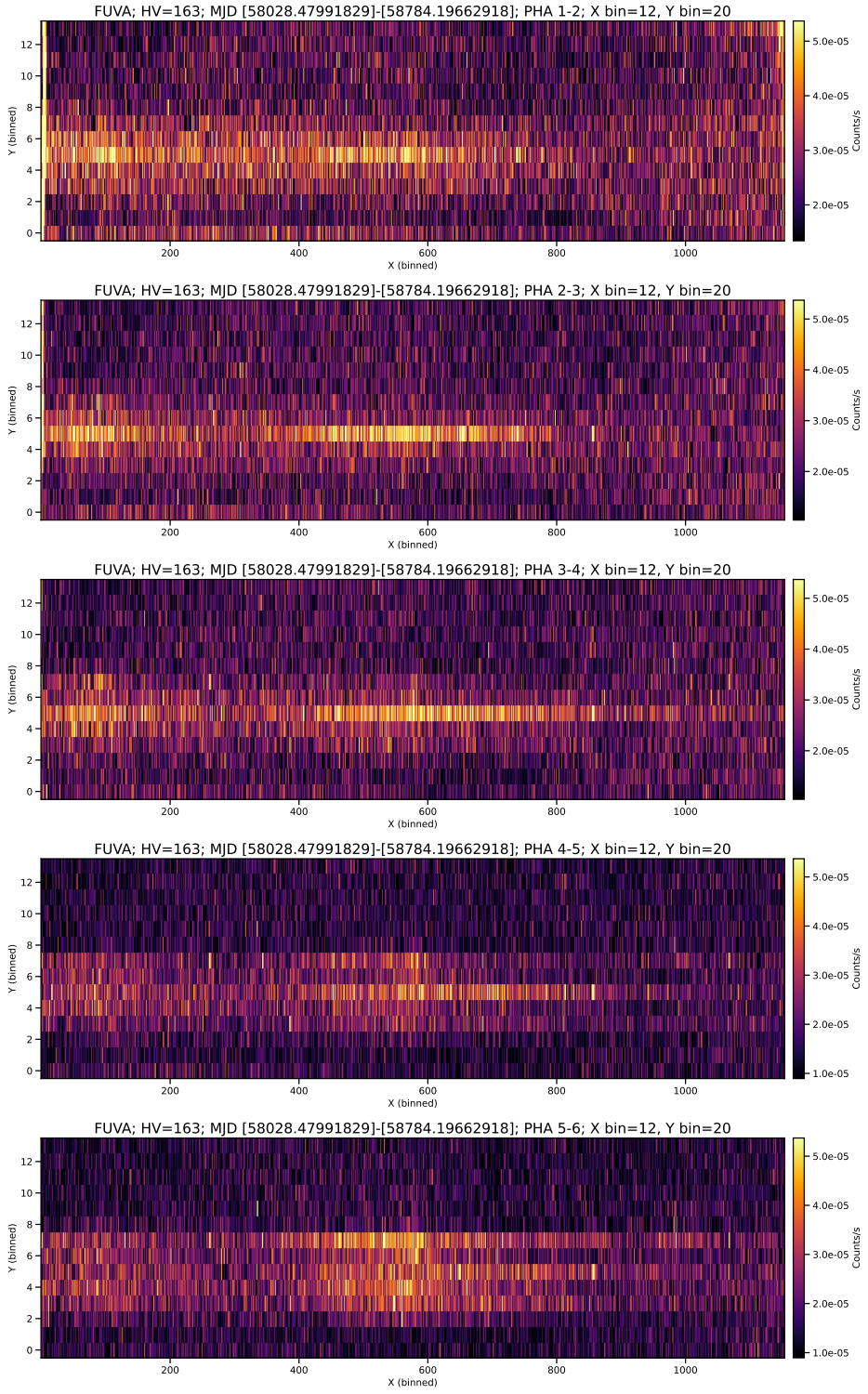

Figure 13. Superdark for segment A, HV=163, state 1. From top to bottom the panels show the distribution of counts for PHAs 1-5.

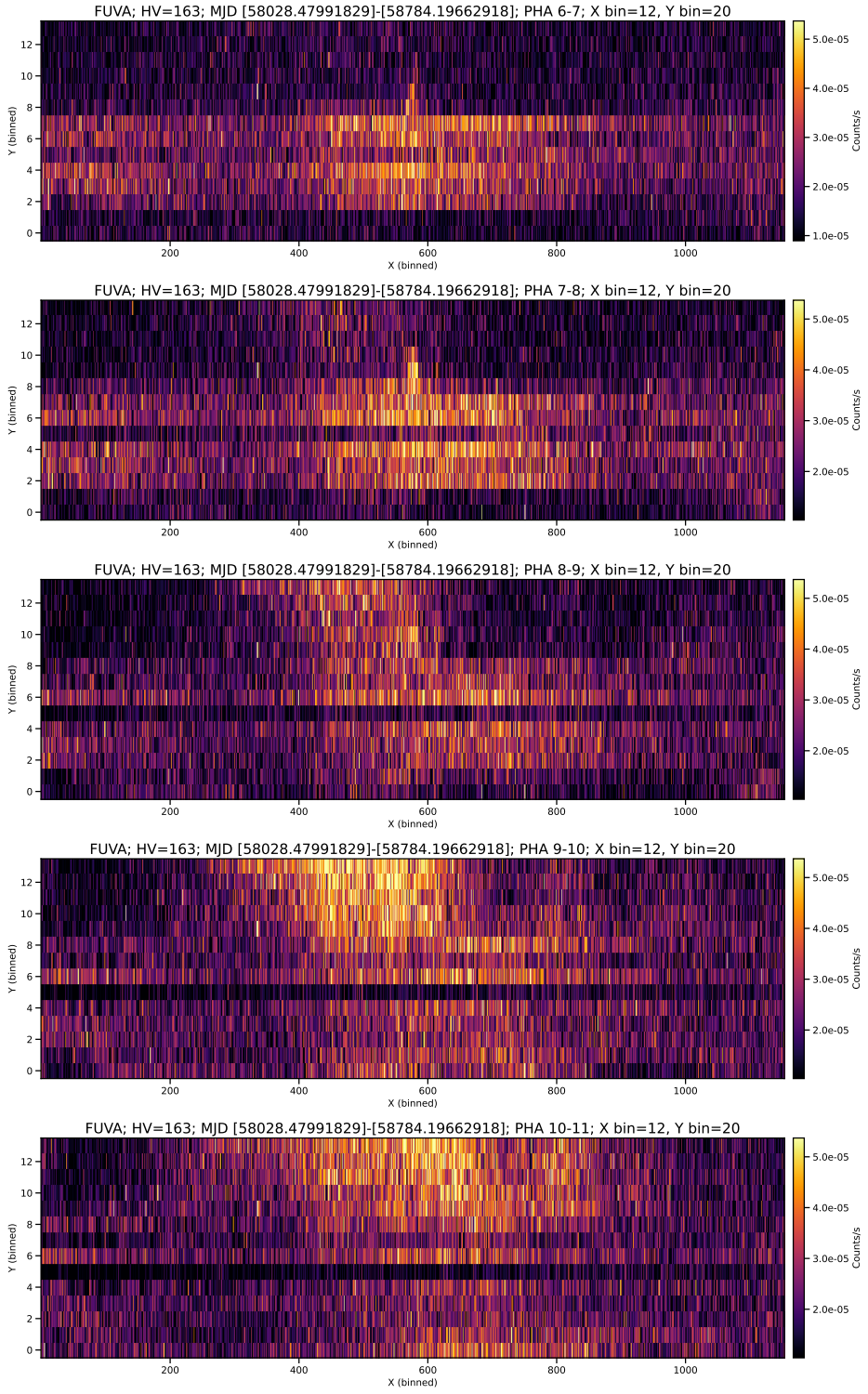

Figure 14. Superdark for segment A, HV=163, state 1. From top to bottom the panels show the distribution of counts for PHAs 6-10.

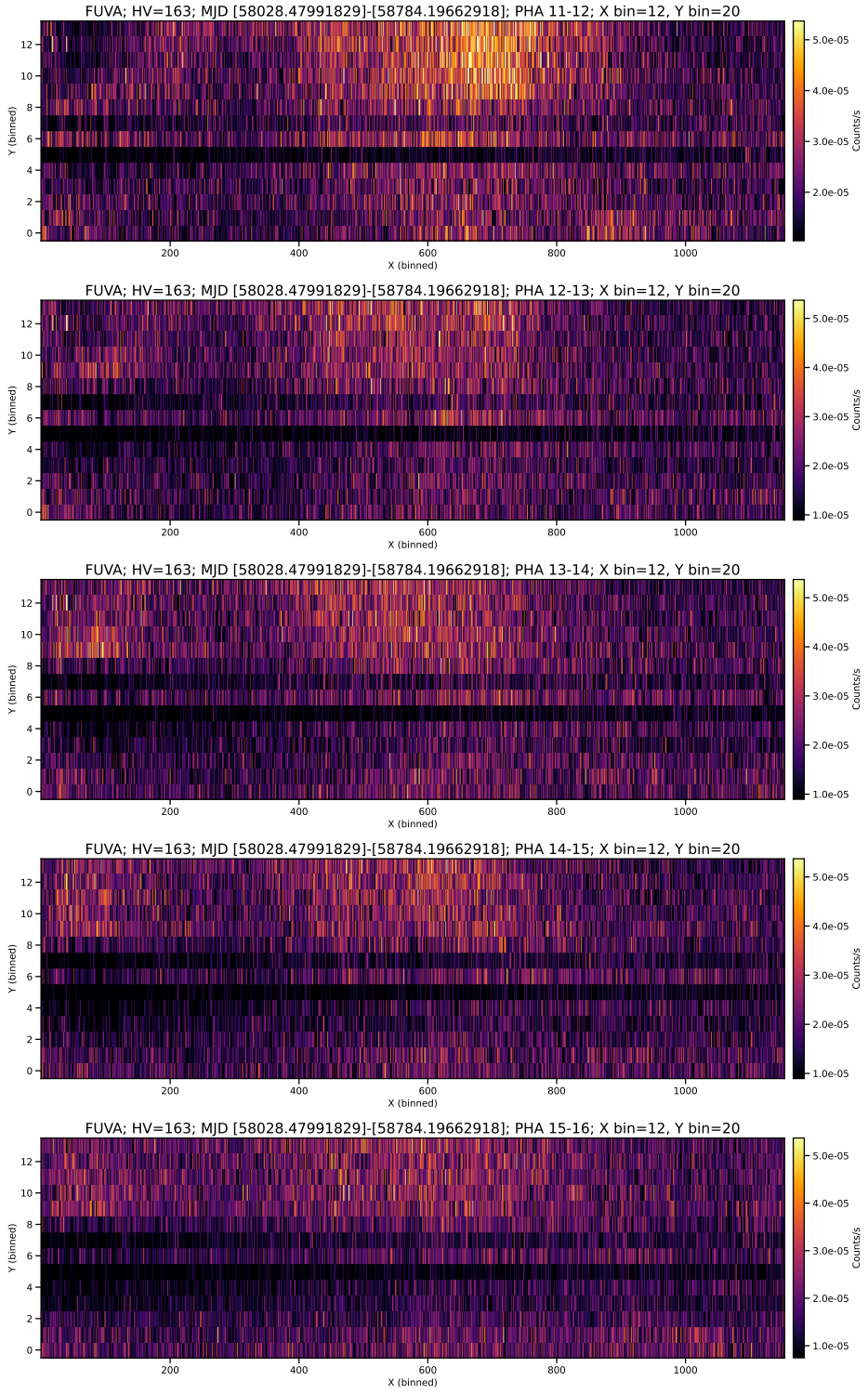

Figure 15. Superdark for segment A, HV=163, state 1. From top to bottom the panels show the distribution of counts for PHAs 11-15.

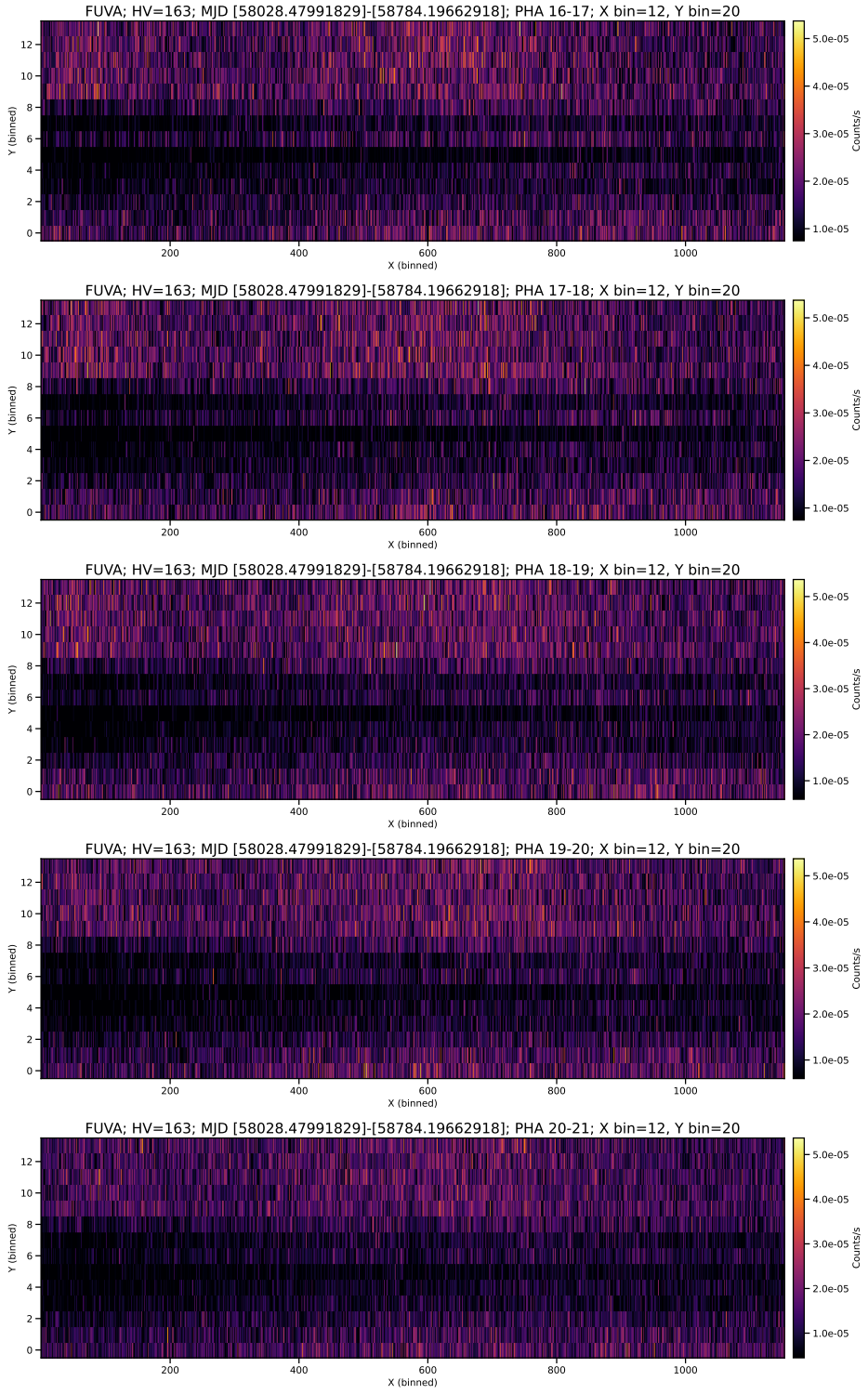

Figure 16. Superdark for segment A, HV=163, state 1. From top to bottom the panels show the distribution of counts for PHAs 16-20.

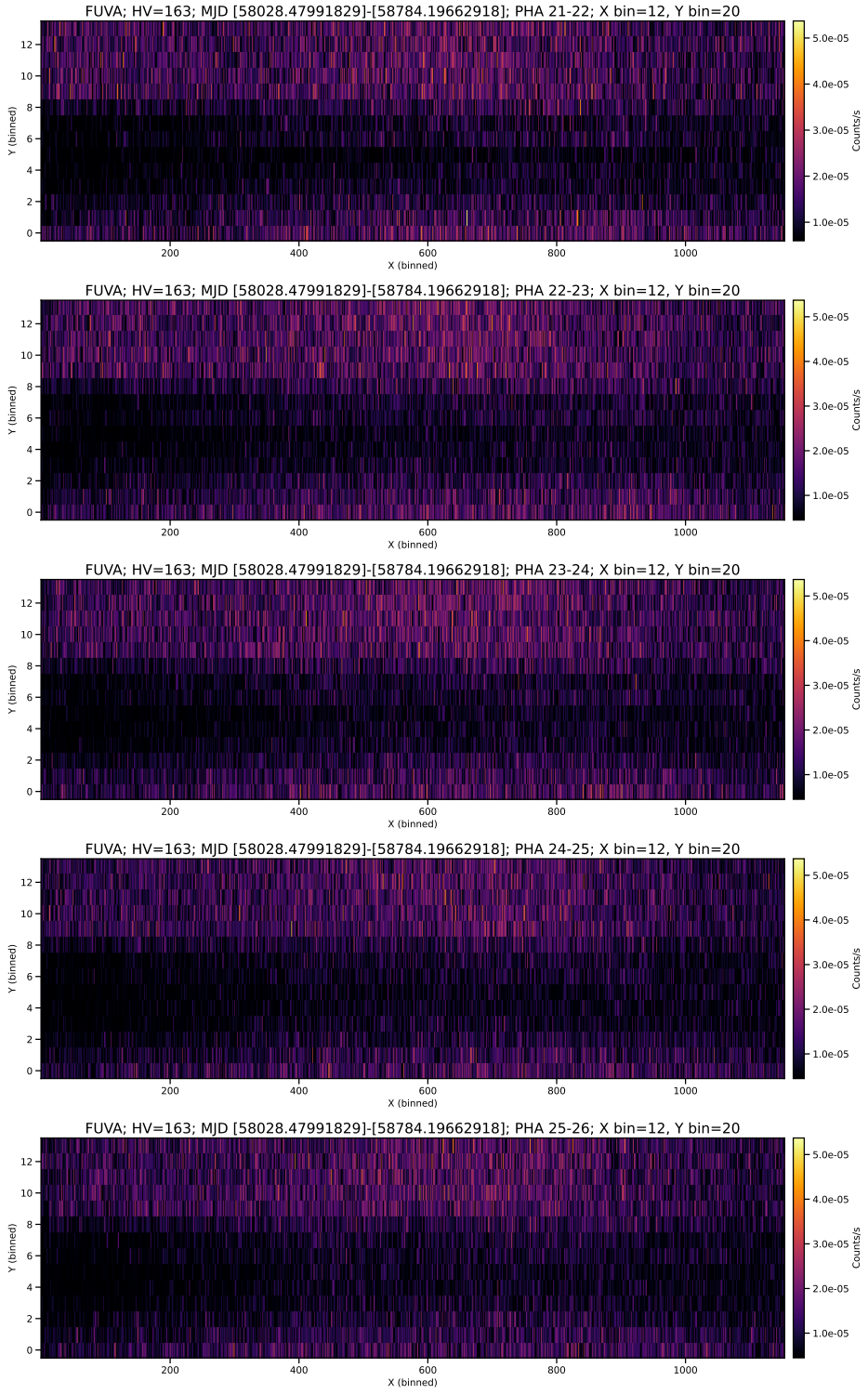

Figure 17. Superdark for segment A, HV=163, state 1. From top to bottom the panels show the distribution of counts for PHAs 21-25.

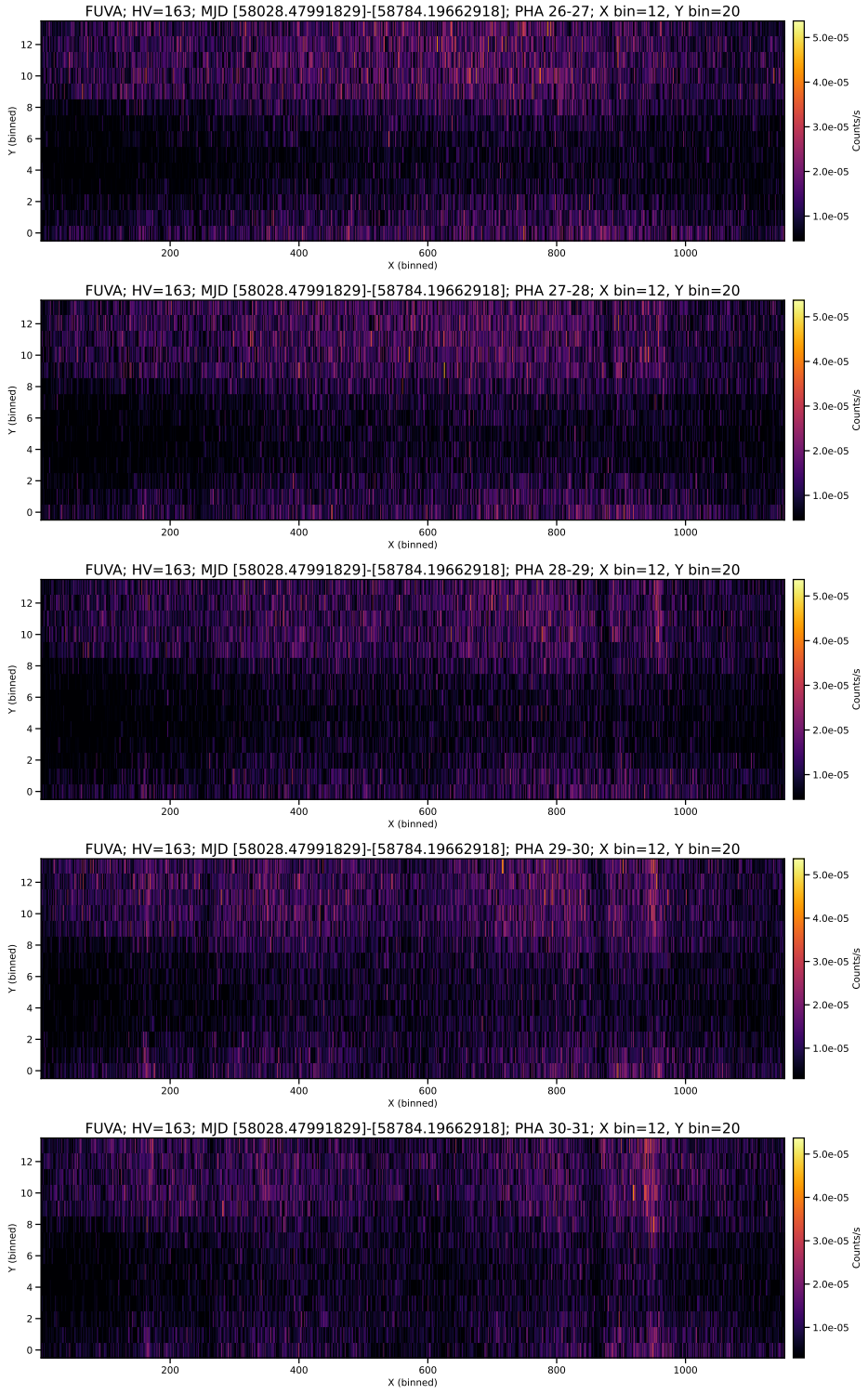

Figure 18. Superdark for segment A, HV=163, state 1. From top to bottom the panels show the distribution of counts for PHAs 26-30. Similar to the "banding/striping" observed in the darks for segment B (Section 1.2), a similar faint structure starts appearing at high PHA values in segment A.

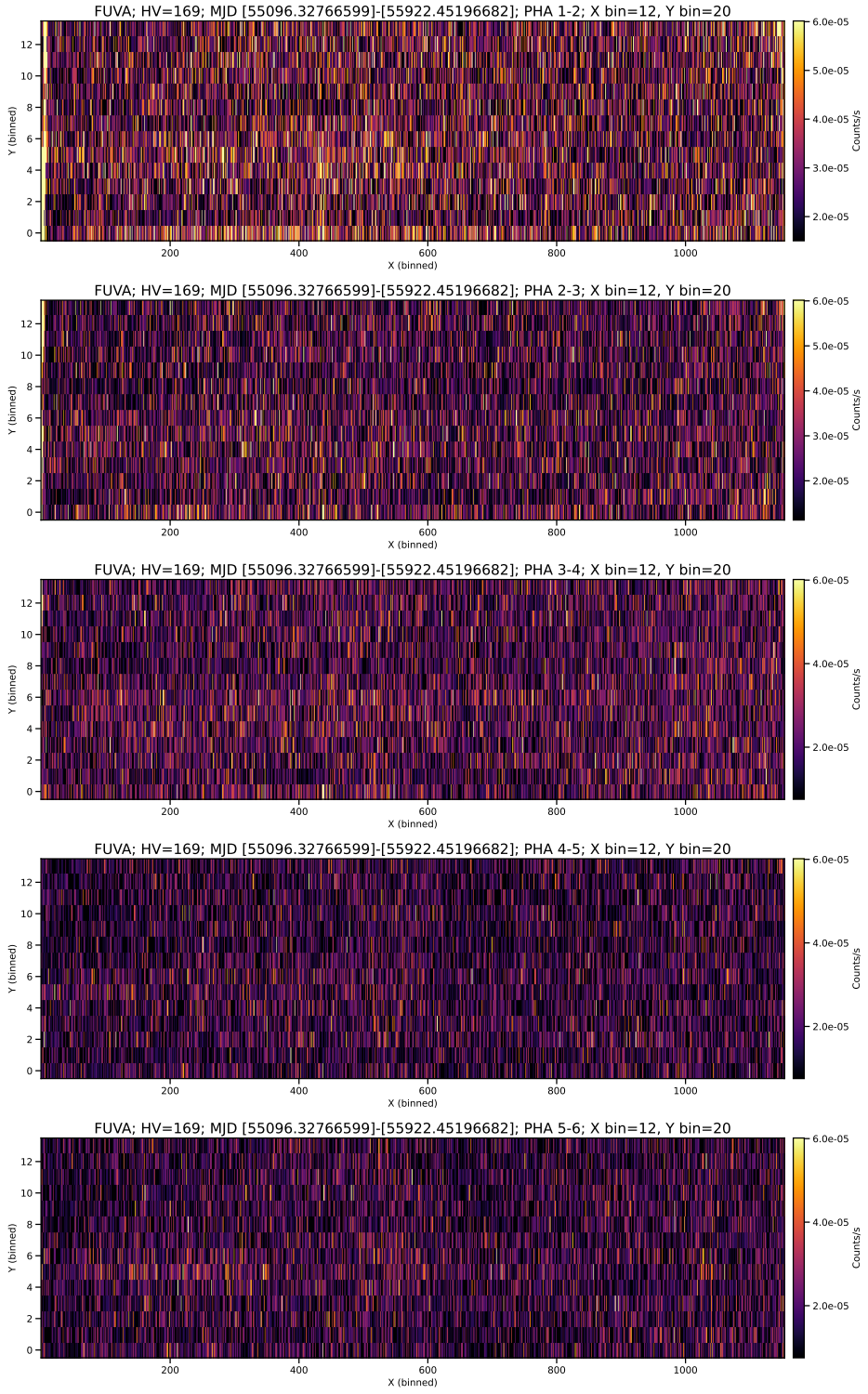

Figure 19. Superdark for segment A, HV=169, state 2. From top to bottom the panels show the distribution of counts for PHAs 1-5.

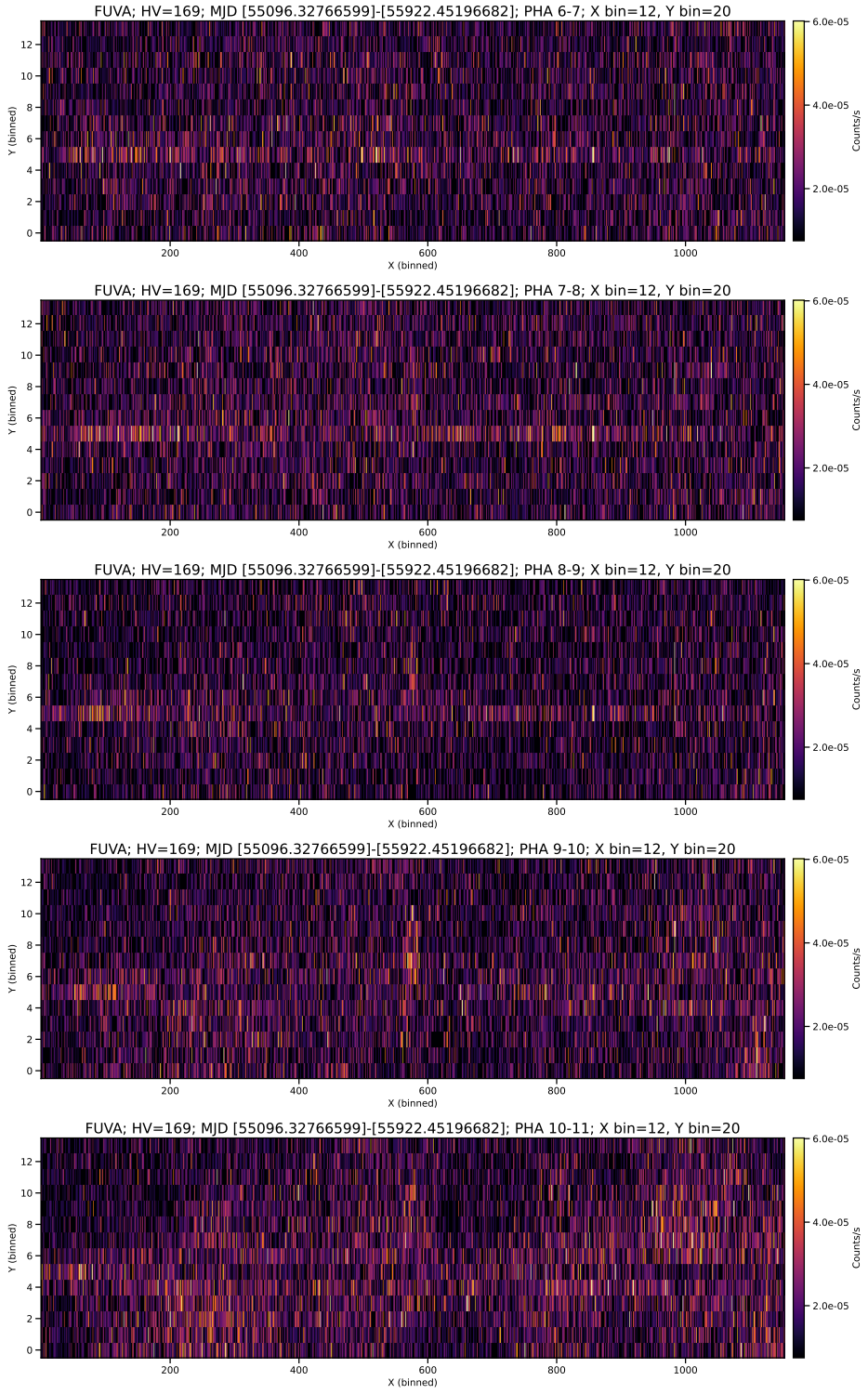

Figure 20. Superdark for segment A, HV=169, state 2. From top to bottom the panels show the distribution of counts for PHAs 6-10.

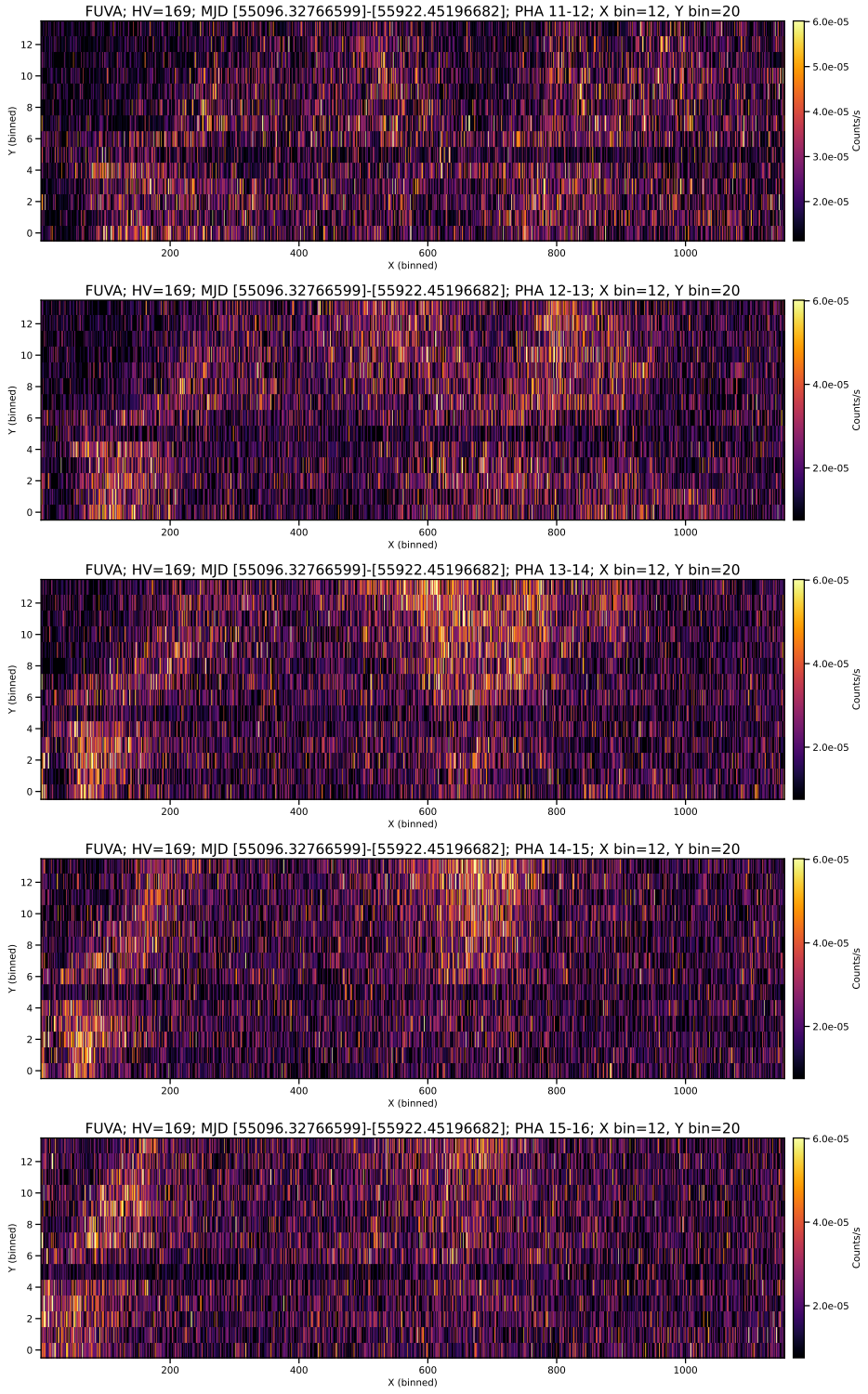

Figure 21. Superdark for segment A, HV=169, state 2. From top to bottom the panels show the distribution of counts for PHAs 11-15. Note the multiple glow features appearing at these PHA values.

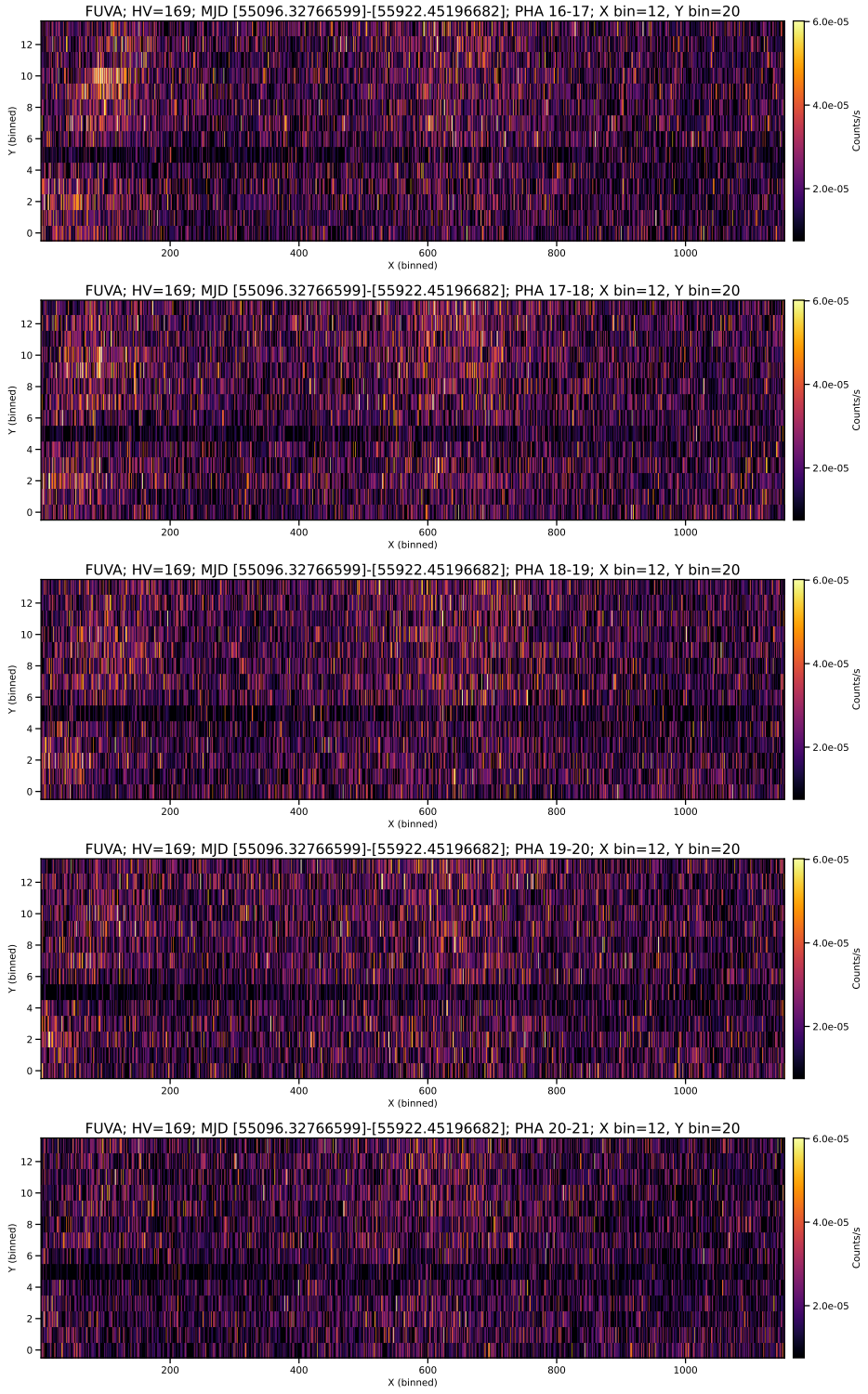

Figure 22. Superdark for segment A, HV=169, state 2. From top to bottom the panels show the distribution of counts for PHAs 16-20. The structures appearing at PHAs 11-15, dissapear for higher PHAs.

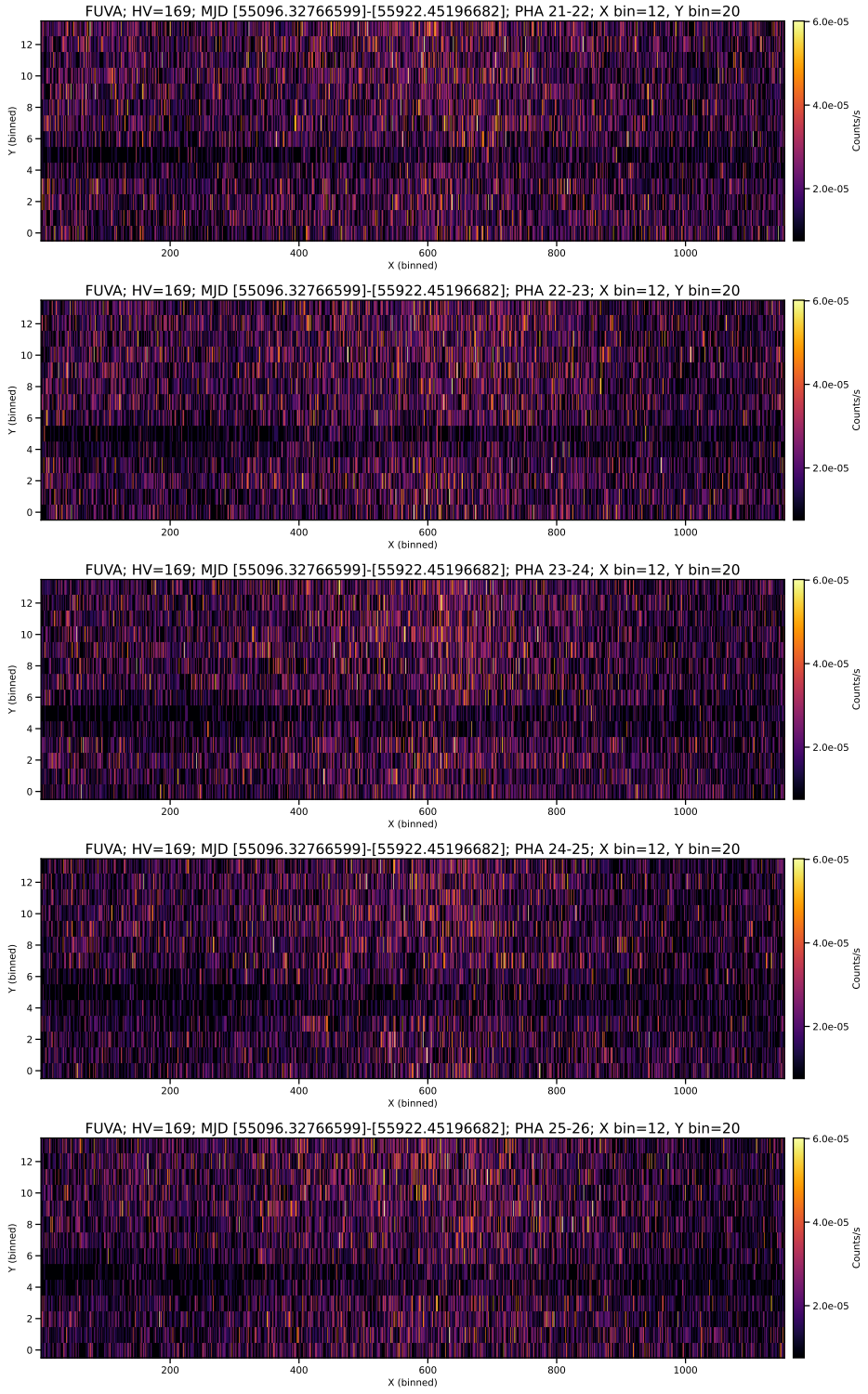

Figure 23. Superdark for segment A, HV=169, state 2. From top to bottom the panels show the distribution of counts for PHAs 21-25.

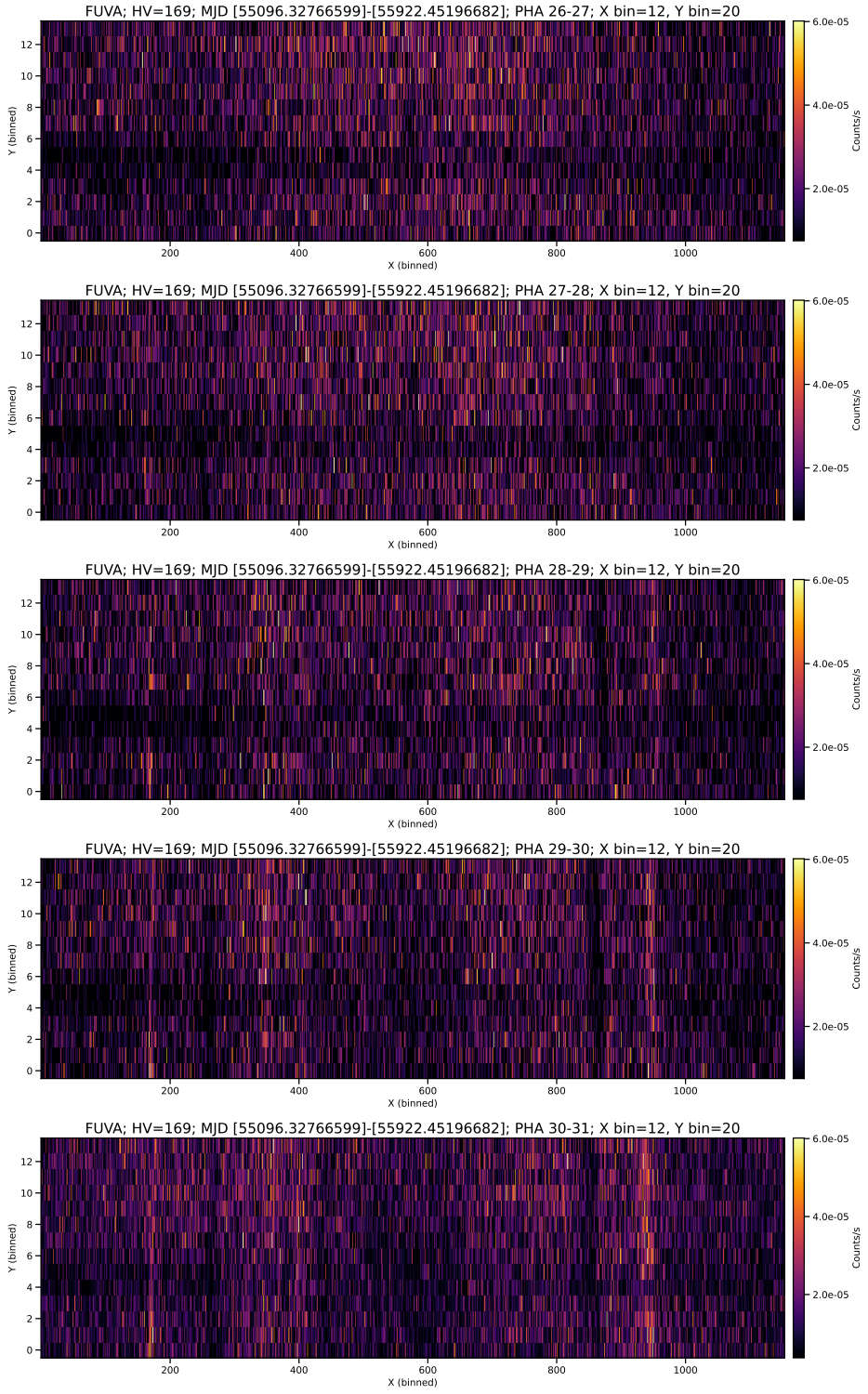

Figure 24. Superdark for segment A, HV=169, state 2. From top to bottom the panels show the distribution of counts for PHAs 26-30. Similar to the "banding/striping" observed in the darks for segment B (Section 1.2), a similar faint structure starts appearing at high PHA values in segment A.

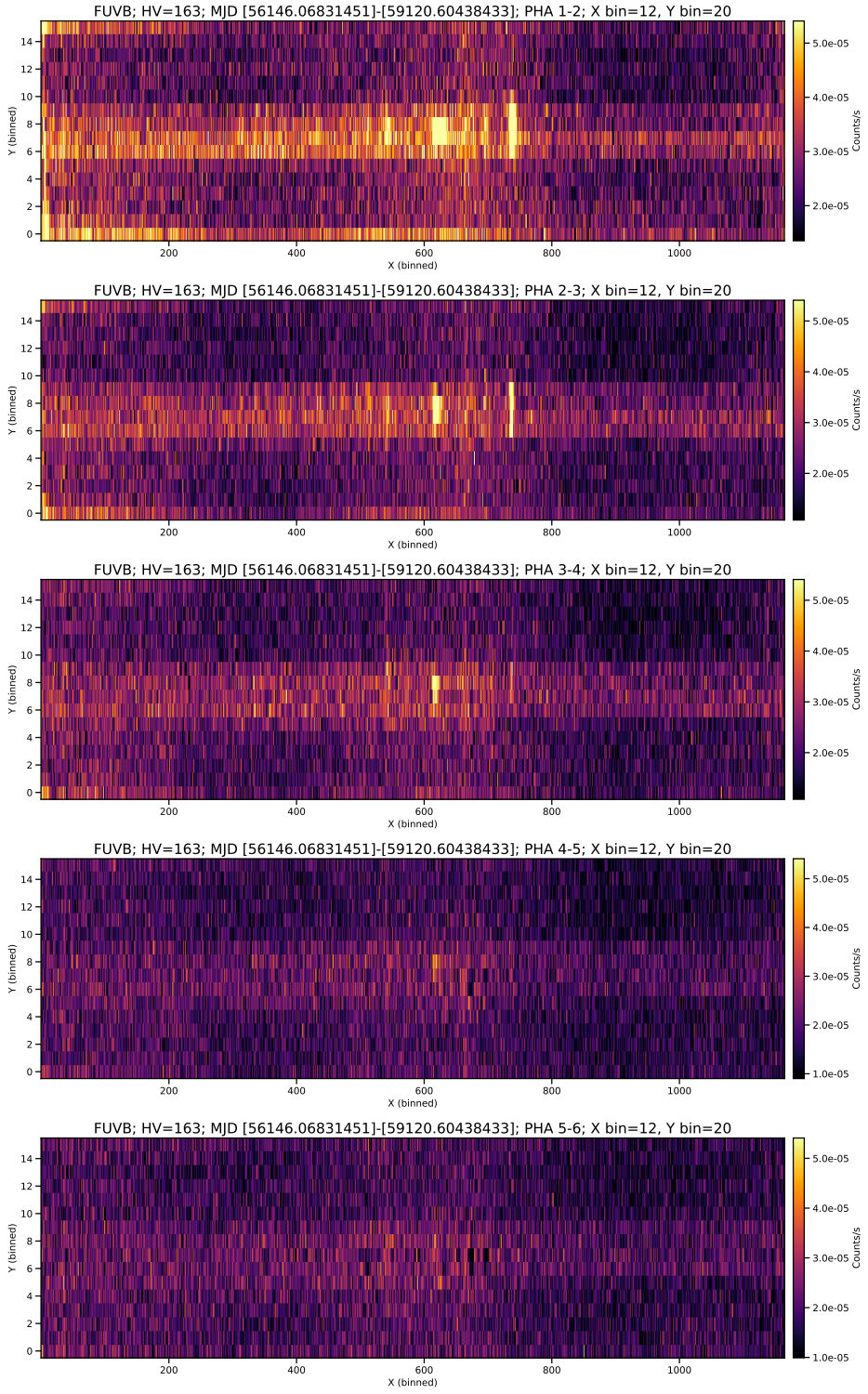

Figure 25. Superdark for segment B, HV=163, state 1. From top to bottom the panels show the distribution of counts for PHAs 1-5.

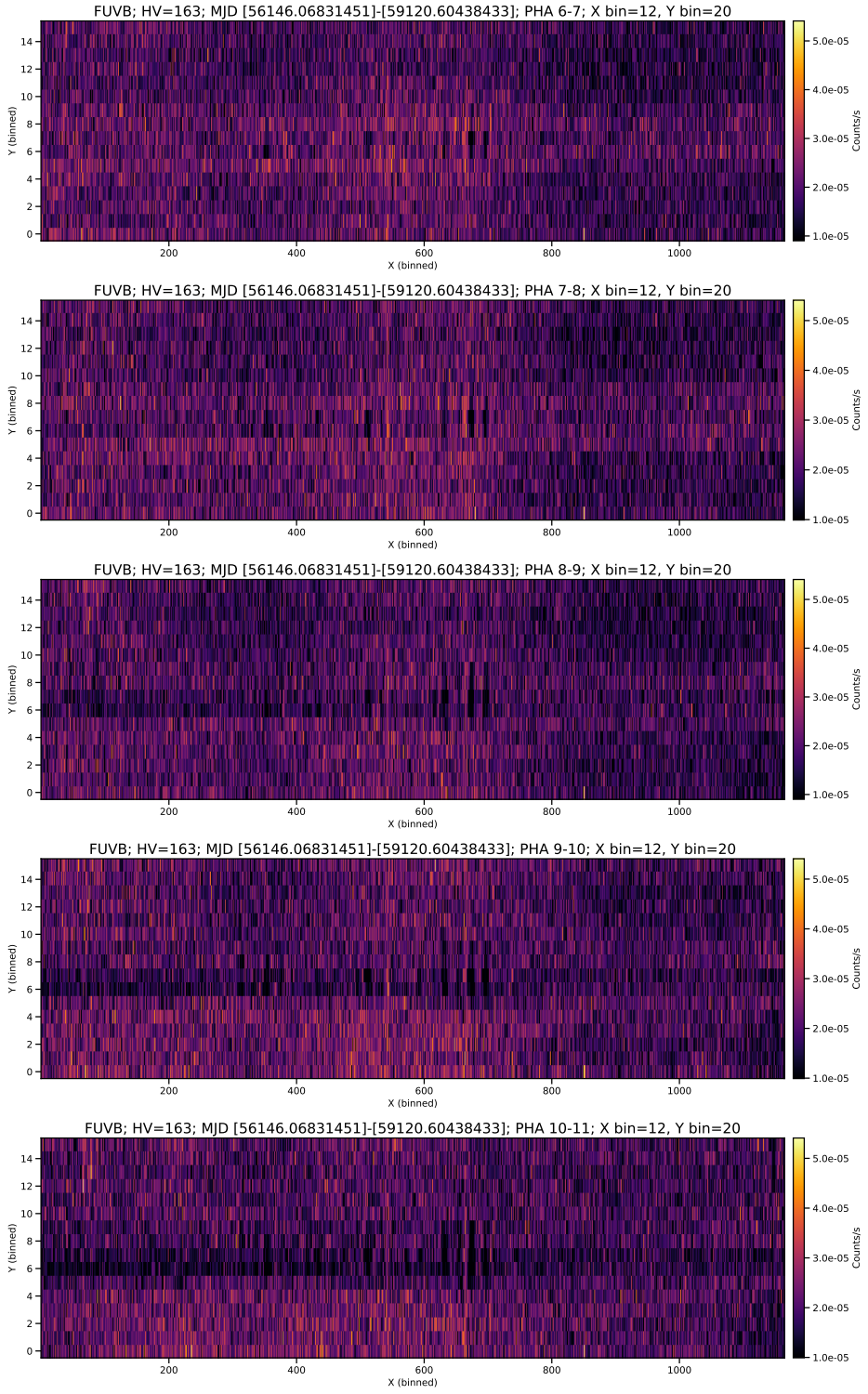

Figure 26. Superdark for segment B, HV=163, state 1. From top to bottom the panels show the distribution of counts for PHAs 6-10.

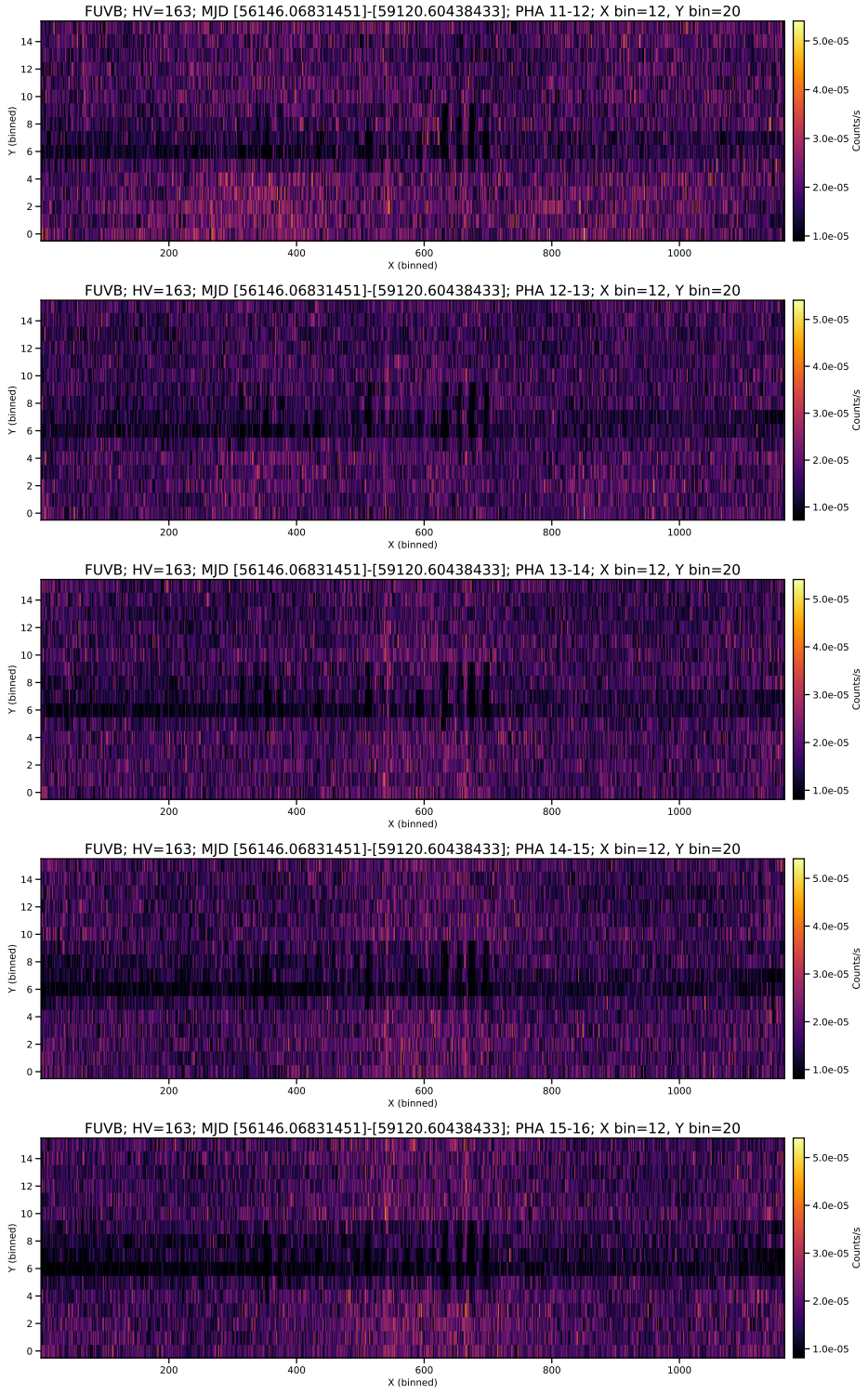

Figure 27. Superdark for segment B, HV=163, state 1. From top to bottom the panels show the distribution of counts for PHAs 11-15.

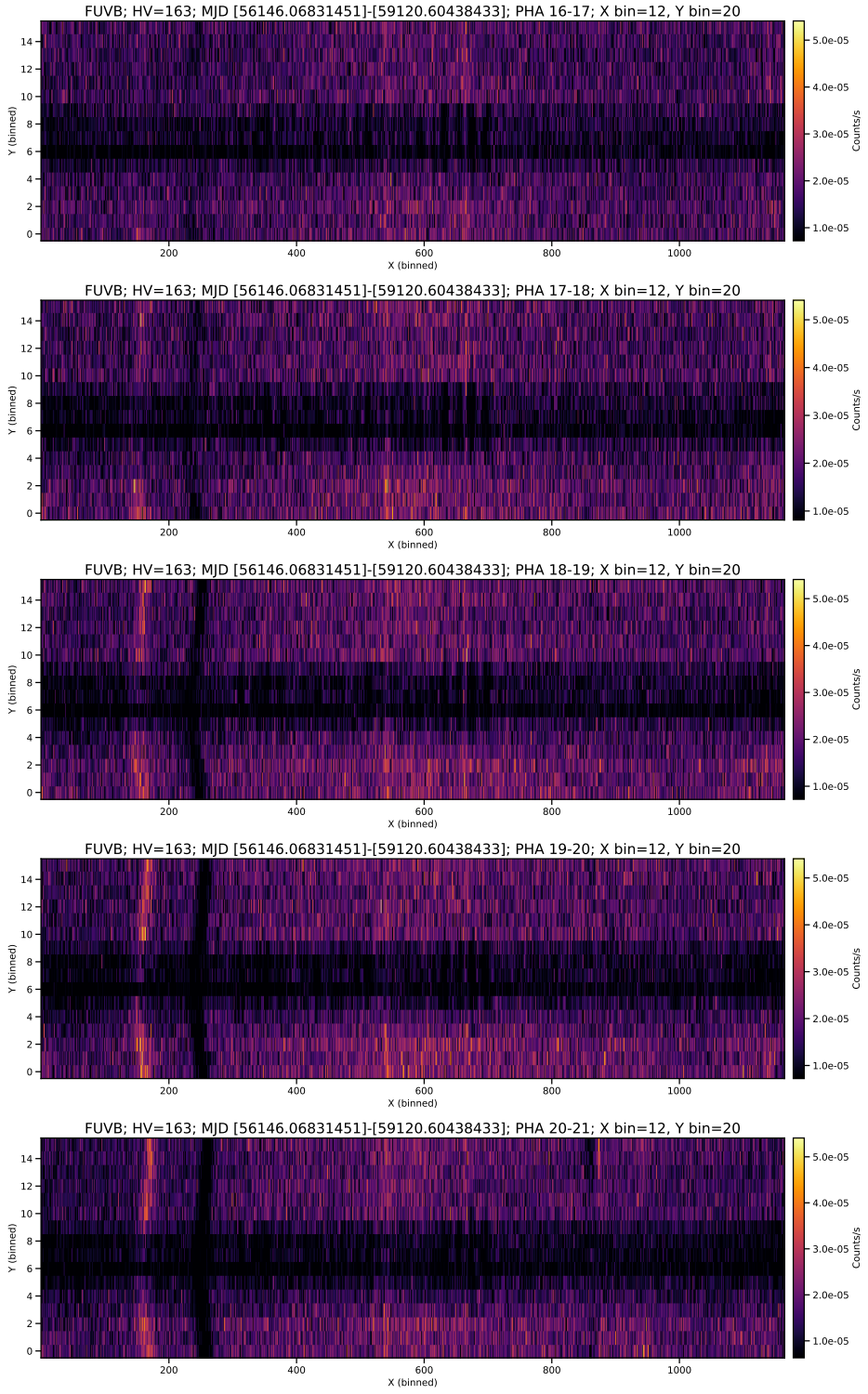

Figure 28. Superdark for segment B, HV=163, state 1. From top to bottom the panels show the distribution of counts for PHAs 16-20. Note the appearance of the "banding/striping" discussed in Section 1.2.

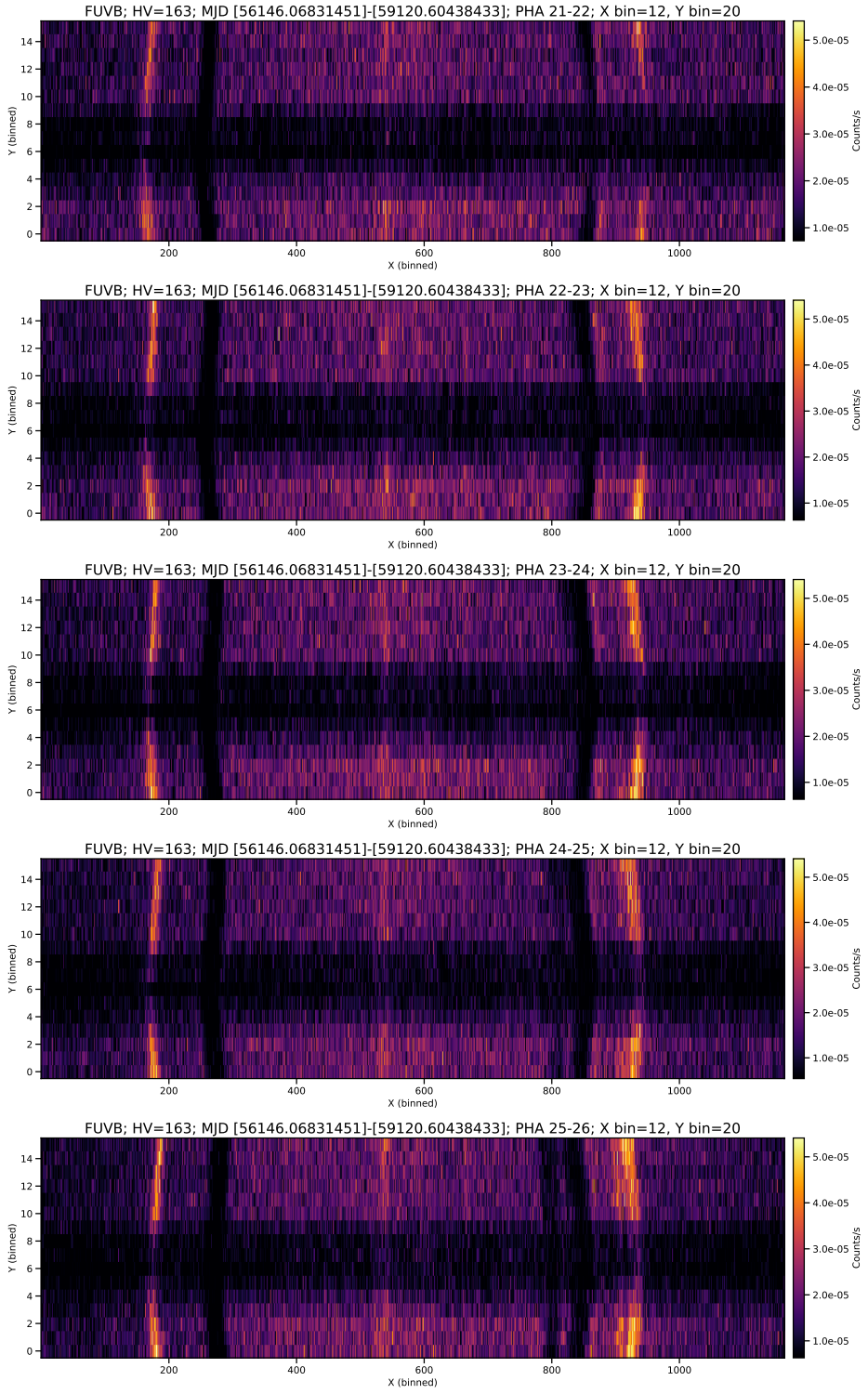

Figure 29. Superdark for segment B, HV=163, state 1. From top to bottom the panels show the distribution of counts for PHAs 21-25. The "banding/striping" structures are stronger at higher PHAs.

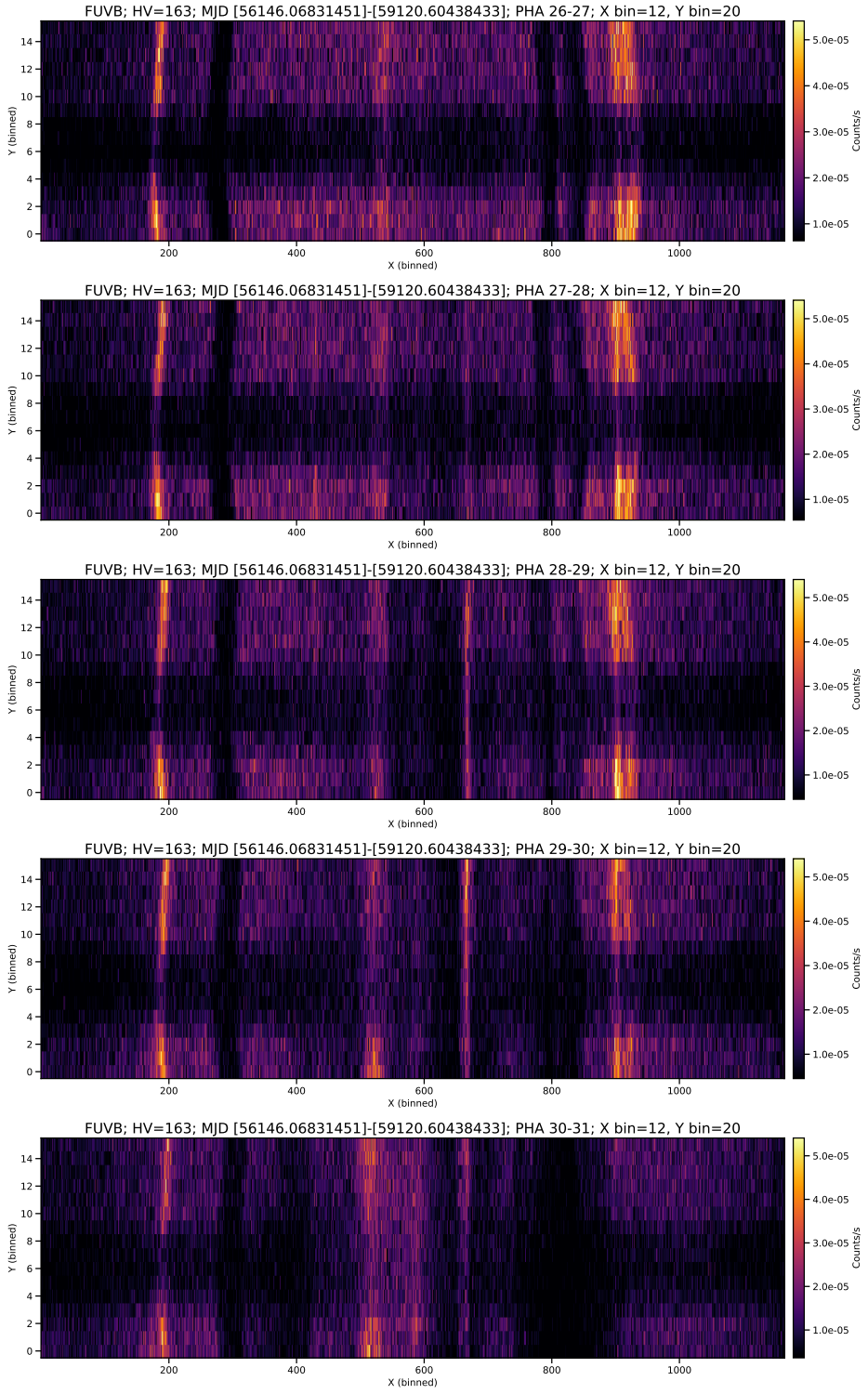

Figure 30. Superdark for segment B, HV=163, state 1. From top to bottom the panels show the distribution of counts for PHAs 26-30.

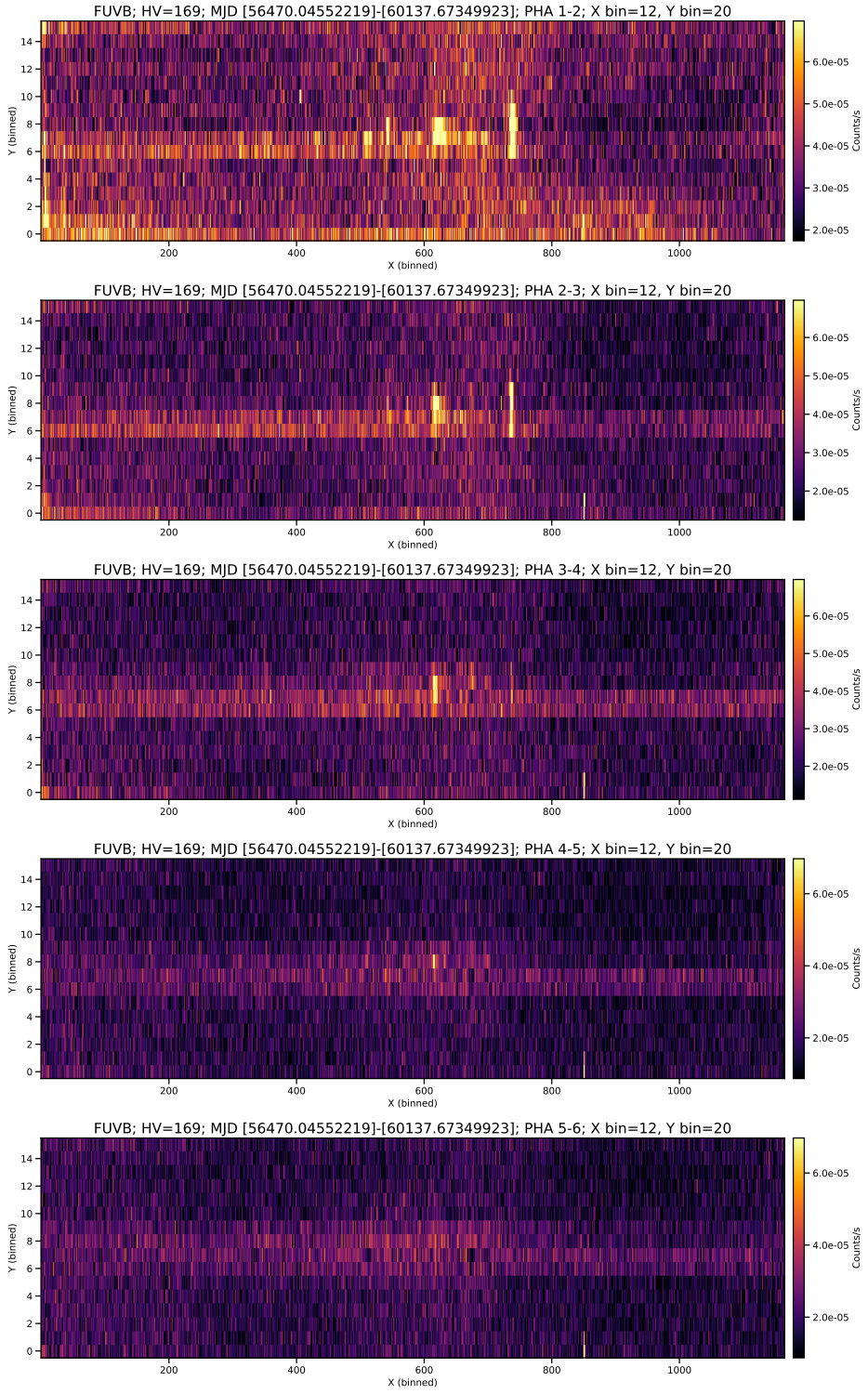

Figure 31. Superdark for segment B, HV=169, state 1. From top to bottom the panels show the distribution of counts for PHAs 1-5.

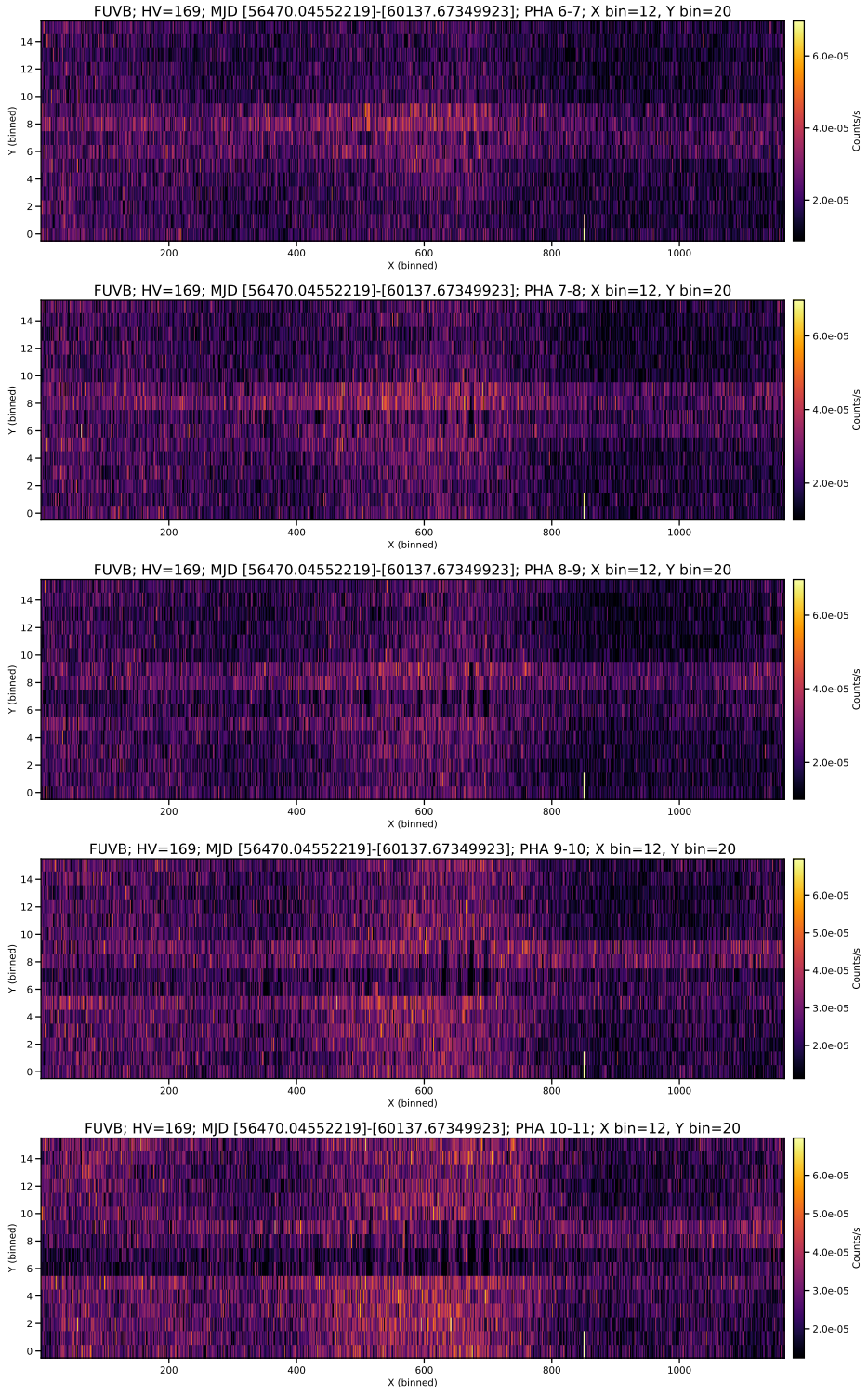

Figure 32. Superdark for segment B, HV=169, state 1. From top to bottom the panels show the distribution of counts for PHAs 6-10.

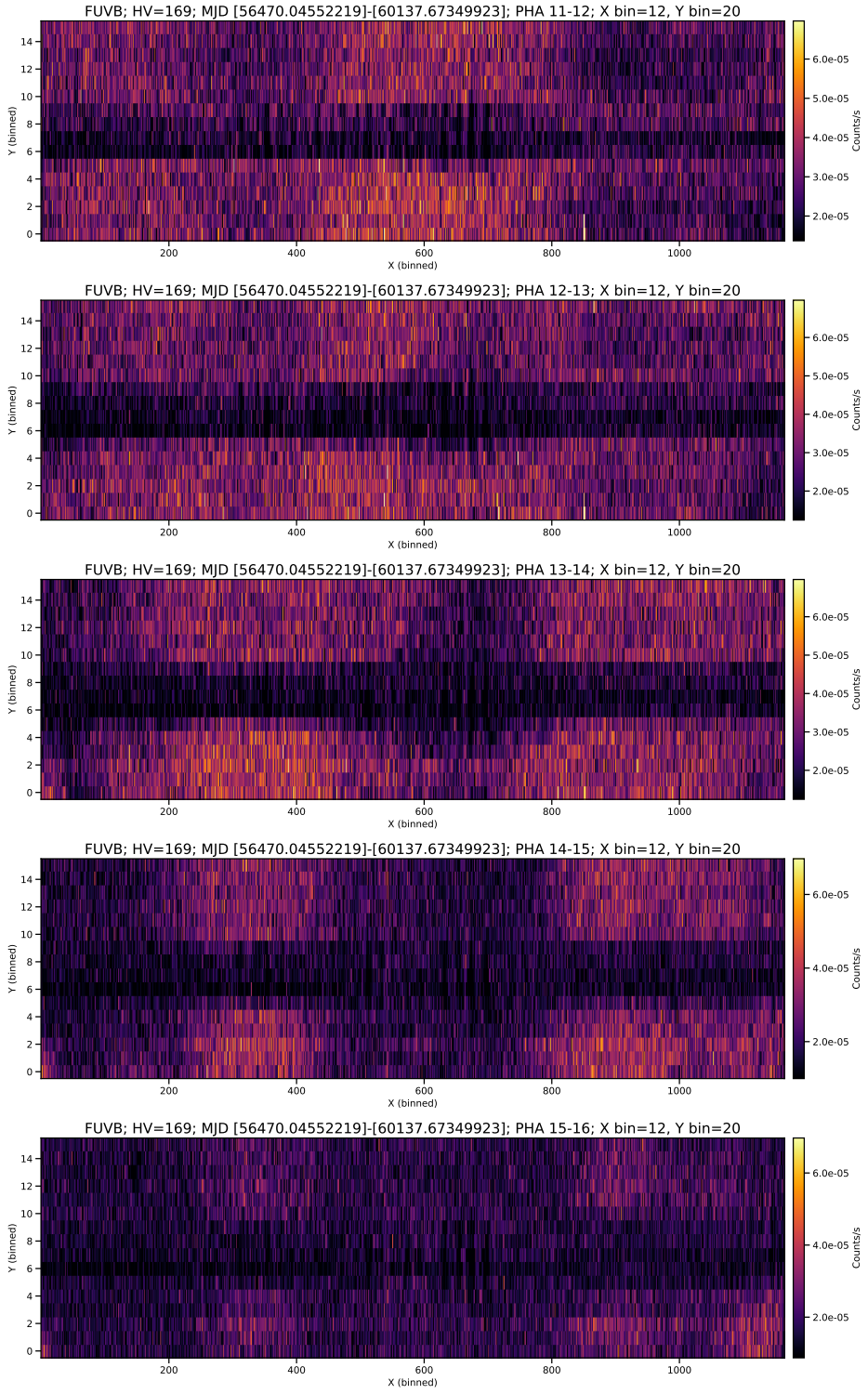

Figure 33. Superdark for segment B, HV=169, state 1. From top to bottom the panels show the distribution of counts for PHAs 11-15.

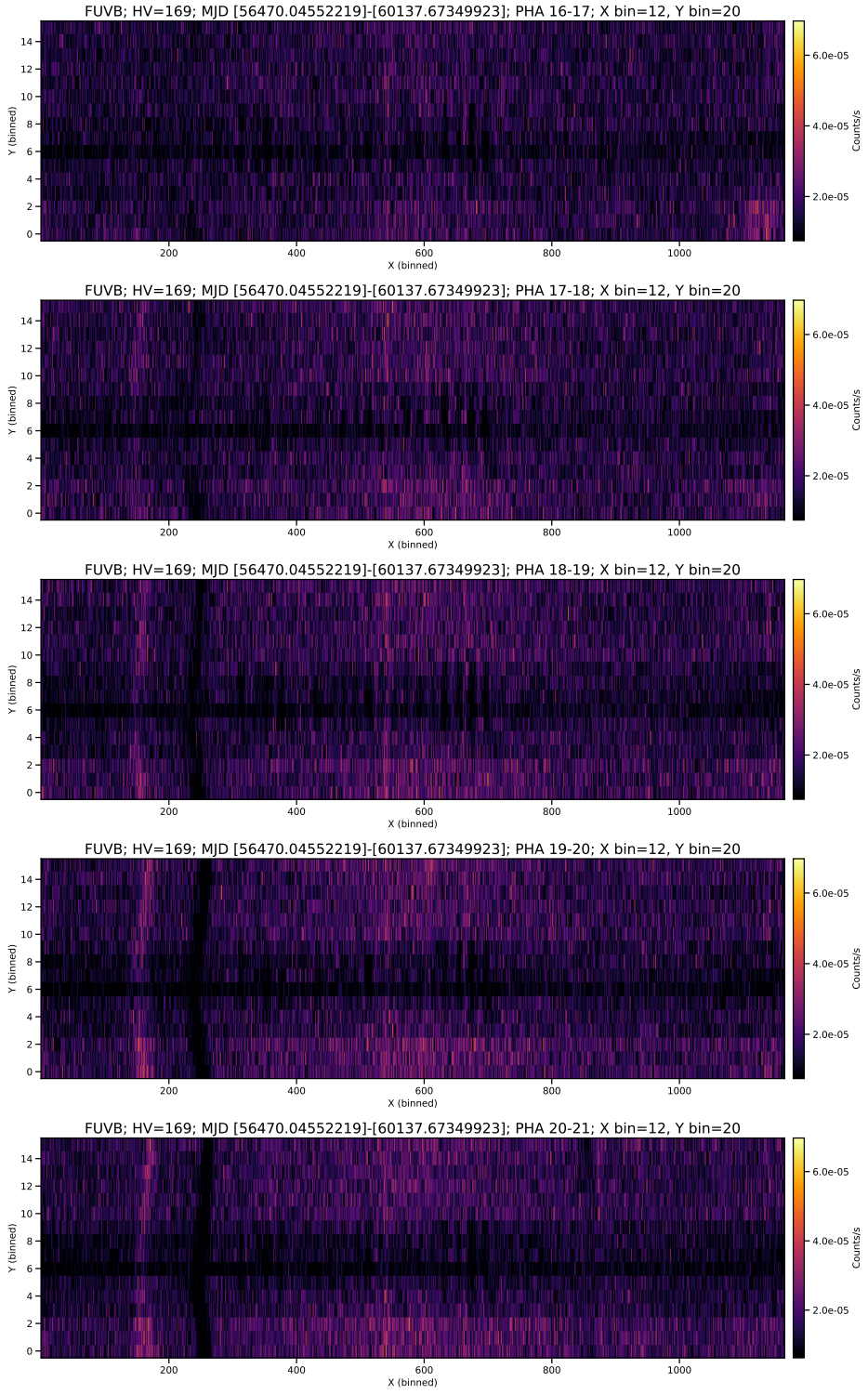

Figure 34. Superdark for segment B, HV=169, state 1. From top to bottom the panels show the distribution of counts for PHAs 16-20.

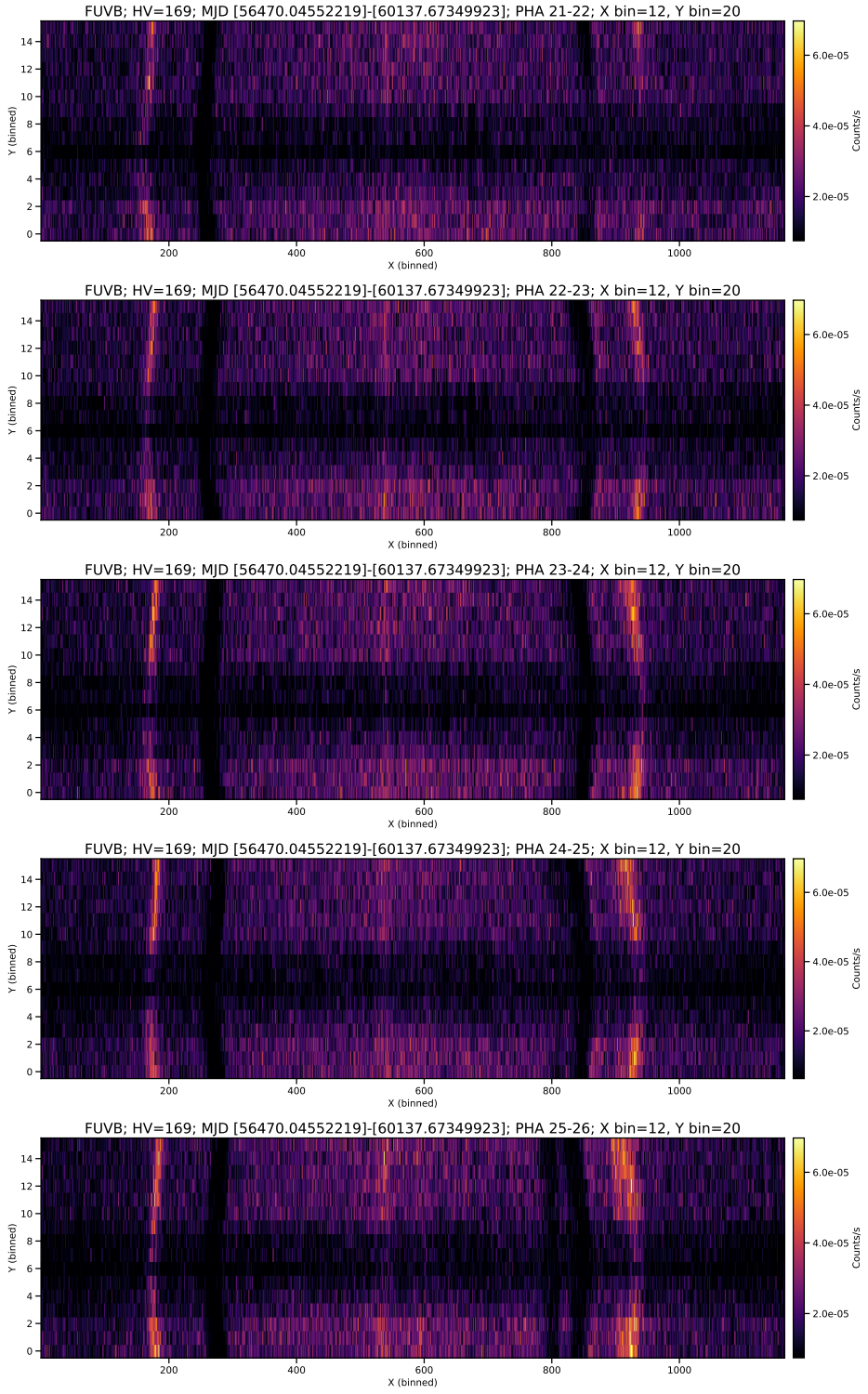

Figure 35. Superdark for segment B, HV=169, state 1. From top to bottom the panels show the distribution of counts for PHAs 21-25.

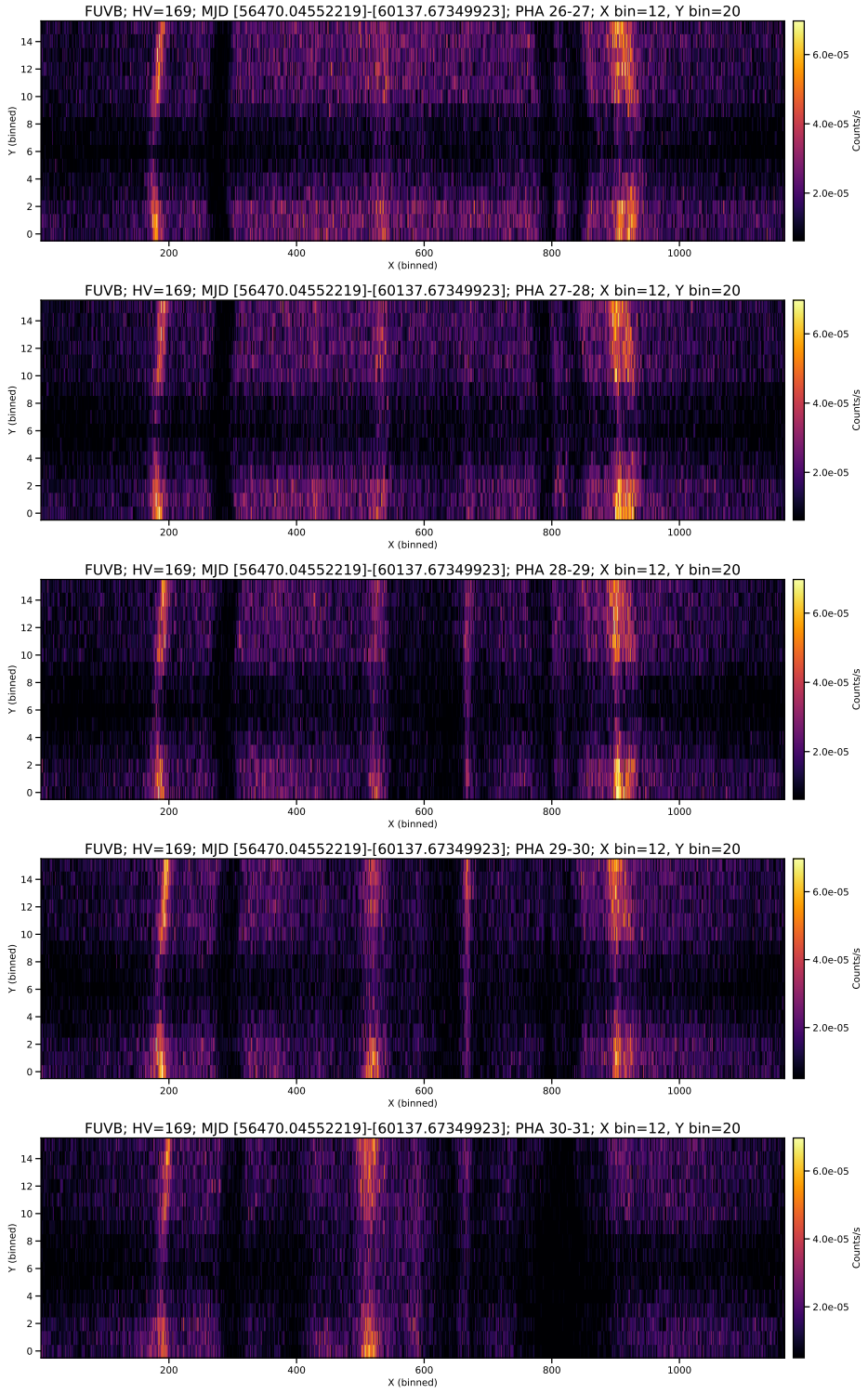

Figure 36. Superdark for segment B, HV=169, state 1. From top to bottom the panels show the distribution of counts for PHAs 26-30.